Reinforcing mechanism of lattice-reinforced cementitious composites insights into flexural performance and material interactions

Zhou, Wen; Bol, Rowin J.M.; Zhou, Yubao; Meng, Zhaozheng; Xu, Yading; Xie, Jinbao; Šavija, Branko

DOI
10.1016/j.matdes.2025.114332

Publication date
2025

Document Version
Final published version

Published in
Materials and Design

Materials & Design 256 (2025) 114332

Contents lists available at ScienceDirect

Materials & Design

journal homepage: www.elsevier.com/locate/matdes

Reinforcing mechanism of lattice-reinforced cementitious composites: insights into flexural performance and material interactions

Wen Zhou *, Rowin J.M. Bol, Yubao Zhou, Zhaozheng Meng, Yading Xu, Jinbao Xie, Branko Šavija

Faculty of Civil Engineering and Geosciences, Delft University of Technology, Delft 2628 CN, the Netherlands

ARTICLE INFO

Keywords:
Lattice-reinforced cementitious composites
Flexural properties
Auxetic
Acoustic emission test
CT scanning

ABSTRACT

Lattice reinforcement (LR) demonstrates great potential in enhancing cementitious matrices due to its ability to be strategically designed and additively manufactured to optimize composite properties. To fully exploit the synergy between LR and cementitious matrix, a deep understanding of the reinforcing mechanisms is essential. In this study, five lattice designs with various configurations and sizes were examined through uniaxial tensile tests on dog-bone specimens. It was observed that geometric characteristics, including auxetic behavior, significantly influenced the mechanical properties of lattice structures. At the composite level, the flexural performance of lattice-reinforced cementitious composites (LRCC) was investigated through four-point bending tests. It was found that up to 23-fold enhancements in energy absorption capacity can be achieved with a low reinforcing ratio of 3.5 %. Acoustic emission tests and CT scanning provided valuable insights into the distinct reinforcing mechanisms between auxetic and non-auxetic lattice designs. Furthermore, Finite Element Method (FEM) simulations confirmed that auxetic LR effectively mitigated interfacial debonding.

1. Introduction

The evolution of advanced composite materials in construction has opened new possibilities for enhancing the performance of cement-based systems. One of the advancements in this area is the integration of lattice structures into cementitious matrices, i.e., lattice-reinforced cementitious composite (LRCC). In recent years, the potential of lattice reinforcements (LR) has attracted increasing interest [1–5], as they tend to exhibit strong deformation capacity paired with relatively low stiffness [6–8]. The ability of the lattice to absorb energy and undergo significant deformation without losing structural integrity complements the natural strengths of concrete, providing a synergistic improvement in ductility and toughness.

Additive manufacturing, in particular, has emerged as a powerful tool for fabricating lattice reinforcements. Lattices can be manufactured with polymer or metal materials, using methods such as fused deposition modeling (FDM) [9–13], powder bed fusion (PBF) (e.g., selective laser sintering (SLS)) [14–16], and stereolithography (SLA) [17–19]. These advanced manufacturing techniques provide unparalleled design flexibility to customize the configurations and geometries of lattice units, e.g., hexagonal, tetrahedral, octet, honeycomb, or a mixed combination. Hence, lattices can be strategically designed and fabricated to optimize composite properties such as strength, toughness, and energy absorption [4,20], offering improvements beyond traditional reinforcement methods. This makes LR a promising solution for a wide range of structural applications, including lightweight structures, impact-resistant systems, and sustainable construction solutions where reduced material usage and enhanced performance are critical.

Among all the lattice designs, auxetic lattices stand out as a particularly unique type – structural metamaterial. Unlike conventional materials which contract laterally when stretched, auxetic lattices exhibit a negative Poisson's ratio, i.e., expanding laterally when subjected to tension and contracting laterally under compression (Fig. 1) [2,8,21,22]. This counterintuitive response is a direct result of their structurally engineered geometries, often comprising chiral [23–27], re-entrant [28–30], or rotational [31–33] units, etc. These geometric features allow for complex deformation patterns, which, when repeated and tessellated to form an auxetic lattice structure, lead to a combination of low weight [34,35], high energy absorption [36,37], superior indentation resistance [38–40], and high shear resistance [41,42].

* Corresponding author.
E-mail addresses: w.zhou-2@tudelft.nl (W. Zhou), r.j.m.bol@tudelft.nl (R.J.M. Bol), y.zhou-16@tudelft.nl (Y. Zhou), z.meng@tudelft.nl (Z. Meng), yadingxu@cqu.edu.cn (Y. Xu), j.xie-1@tudelft.nl (J. Xie), b.savija@tudelft.nl (B. Šavija).

https://doi.org/10.1016/j.matdes.2025.114332
Received 13 February 2025; Received in revised form 10 June 2025; Accepted 29 June 2025
Available online 30 June 2025

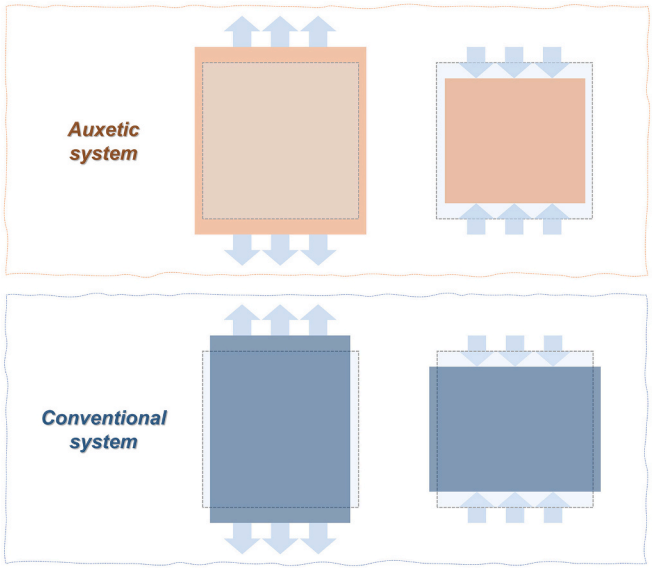

Fig. 1. Schematic diagram of auxetic and conventional structures under tension and compression.

Compressive behavior of cement-based composites has been demonstrated to improve with 3D-printed LR, especially in the case of auxetic lattice structures [2,43]. Previous research has highlighted the effectiveness of negative Poisson's ratio reinforcements for providing confinement to concrete or mortar [20], thereby contributing to composites' ductility or strength, if not both. Xu and Šavija [44] reported that 3D-printed polymer auxetic reinforcements increased the compressive energy absorption by up to 9.53 times compared to unreinforced mortar. This significant enhancement was attributed to the lateral contraction of the planar auxetic structures, which provided in-plane confinement to the mortar and therefore limited post-peak crack propagation. Similarly, Choudhry et al. [45] observed that auxetic lattices led to a 9-fold increase in energy absorption of composites. In both studies, a slightly reduced compressive strength was observed due to the addition of polymer reinforcements, indicating a trade-off between strength and ductility. However, simultaneous enhancements in both strength and ductility were also reported [5,46,47]. This variability in results highlights the importance of proper lattice design to achieve the desired balance between strength and ductility.

Another key focus of LRCC research is flexural performance, as lattice reinforcement has been shown to effectively enhance the ductile response of cementitious composites under bending. In existing flexural studies, lattice reinforcement configurations generally fall into three categories: thin planar structures [11,25,48,49], planar structures connected by out-of-plane trusses/encased by side surface [4,50,51], and three-dimensional structures [52–54]. The first type is usually tested with thin beam specimens, thus occupying a considerate volume fraction. In such cases, multiple cracking and flexural hardening were witnessed with certain lattice designs and material combinations, as reported in [11,25]. Nonetheless, one example with smaller reinforcing

Table 1
Properties of base resin material provided by the manufacturer.

Tensile strength at yield (MPa)	Tensile strength at break (MPa)	Tensile modulus (MPa)	Elongation at break (%)	Solid density (g/cm^3)
44 ± 1	45 ± 2	1434 ± 80	101 ± 11	1.121

Table 2
Printing parameters for lattice structures.

Layer thickness (μm)	Layer exposure time (s)	Bottom layer exposure time (s)	Bottom layer number	Light-off delay (s)
50	12	35	8	6.5 s

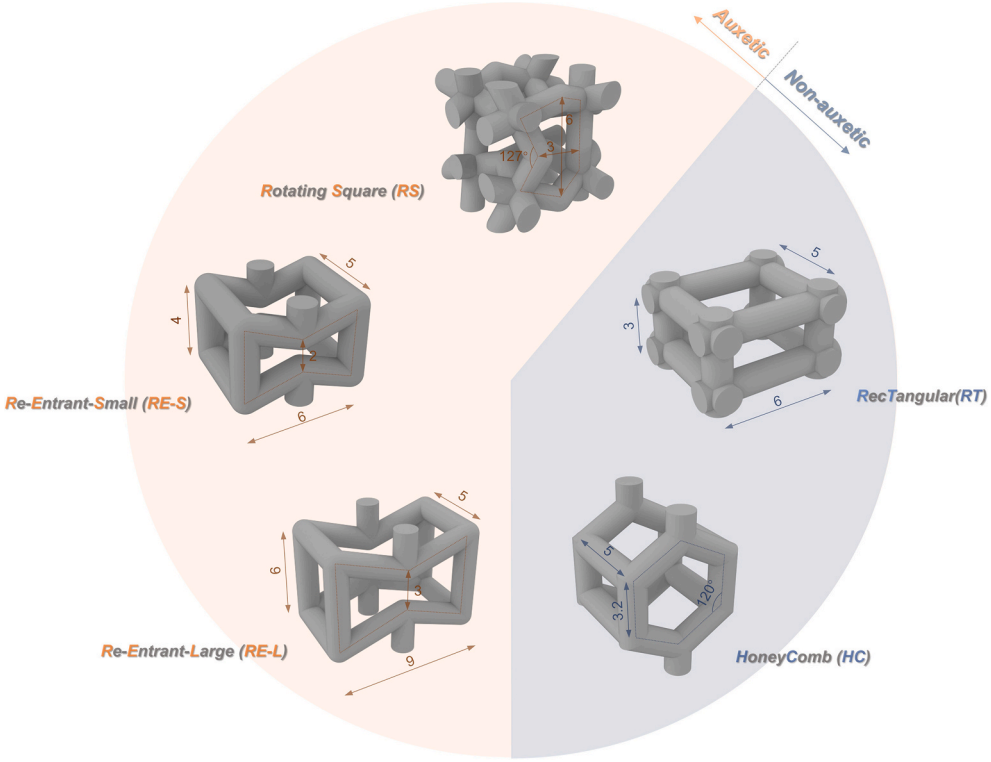

Fig. 2. Lattice designs and geometries (unit: mm). All dimensions are measured based on skeleton lines. Each strut has a diameter of 1.5 mm.

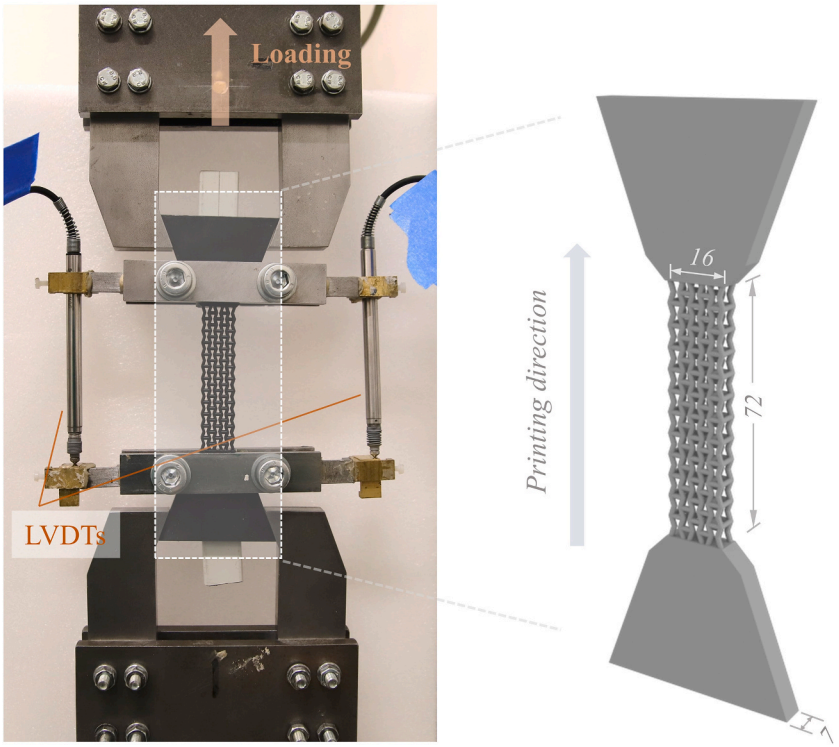

Fig. 3. Setups and sample geometries of uniaxial tensile tests.

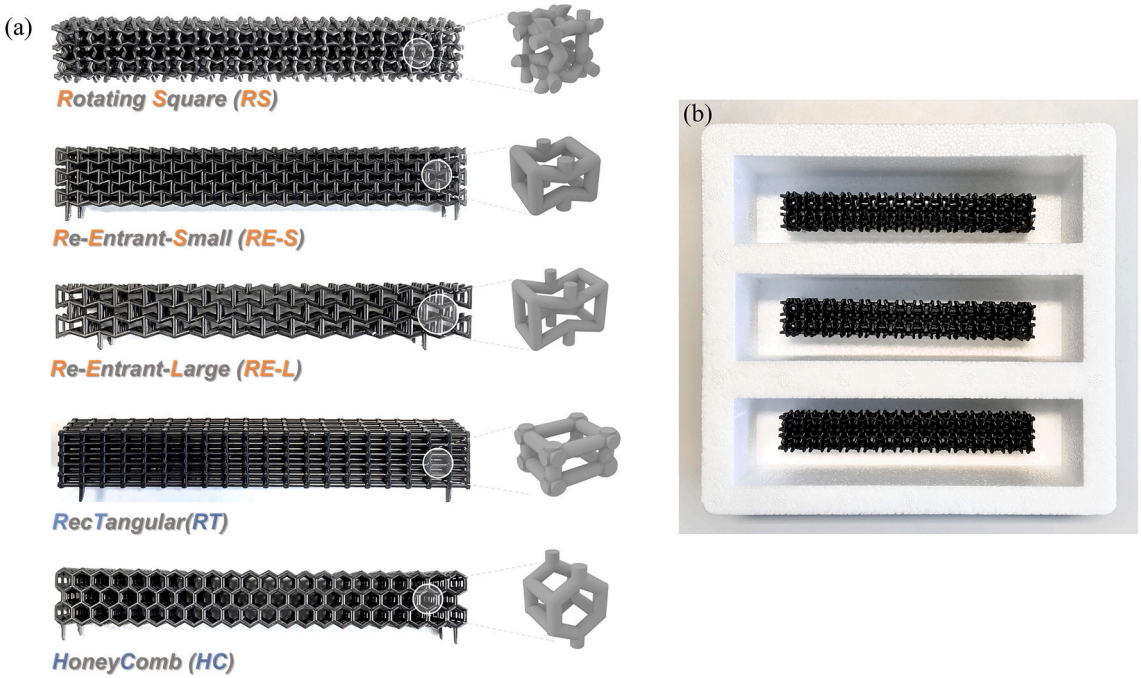

Fig. 4. (a) 3D printed lattice reinforcements and (b) reinforcements glued in molds before mortar casting.

ratio as shown in [49], where 3D-printed thin lattice plates (3 mm thick) were inserted into specimens of 50 mm height at approximately mid-height, showed flexural softening behavior. Furthermore, in LRCCs with the latter two configurations, which typically aim at superior (pseudo) flexural-hardening behavior, the volume fraction of lattice reinforcement also generally ranges from 20 % to 50 % [4,53,55,56], raising concerns about material usage and sustainability, particularly as LR is often made from polymer materials.

Topology optimization offers a potential approach to lowering the reinforcement ratio while maintaining desired ductility by efficiently allocating material to critical load-bearing locations. With this strategy, Dong et al. [53] reduced the volume fraction of lattice reinforcement to 18 %. However, this resulted in wider main cracks and lower strength compared to materials with higher reinforcement ratios. Xie et al. [54] suggested that, based on simulation results, achieving global ductility at a volume fraction as low as 8.3 % is possible. While these findings offer

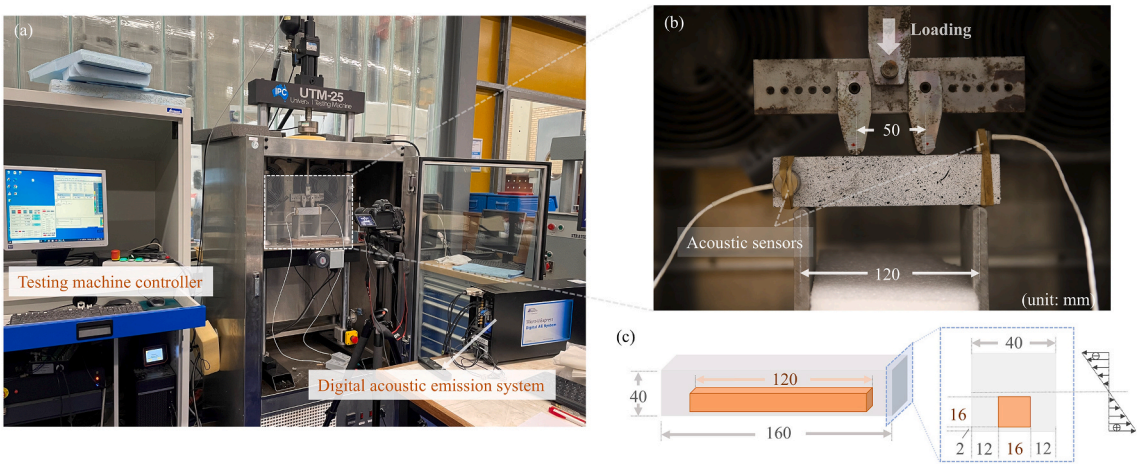

Fig. 5. (a-b) Setups and (c) sample geometries of four-point bending tests and acoustic emission tests. The orange prism in (c) represents the outline of lattice reinforcement. (For interpretation of the references to color in this figure legend, the reader is referred to the web version of this article.)

Table 3
Mix proportions of cementitious matrix (Unit: kg/m^3).

OPC	FA	Sand	Water	SP
473	559	473	413	2.0

Note: OPC: ordinary Portland cement; FA: fly ash; SP: superplasticizer.

hope for reducing material usage, the effectiveness of such low reinforcement ratios has yet to be experimentally validated. Moreover, the underlying reinforcing mechanism at small reinforcement fractions remains unclear.

In addition, while extensive research has been conducted on auxetic lattice-reinforced composites under compression, studies examining their tensile and flexural performance remain limited [25,49,51]. Specifically, there is a lack of in-depth investigation and explanation of the working mechanisms within the composites, particularly concerning the interaction between the auxetic LR and the surrounding cementitious matrix. Key interfacial phenomena, such as debonding, sliding, and the overall load transfer between the auxetic reinforcement and the matrix, have not been comprehensively studied. Understanding these interactions is essential for improving the composite's performance and providing valuable insights into how to effectively utilize the auxetic lattice structure's special characteristics in cementitious composites.

To fill the identified research gap, this study investigated the tensile response of five different lattice designs with various configurations and sizes and probed the flexural behavior of LRCCs with a low reinforcing ratio (2.5 %−3.8 %). Non-destructive damage monitoring techniques, acoustic emission test and micro-CT scanning, were deployed to characterize the damage progression and interaction mechanisms between LR and cementitious matrix. In addition to experimental investigations, Finite Element Method (FEM) simulations were performed to probe the deformation mechanism of LR and the composite behavior of LRCCs.

2. Experimental programs

2.1. Architected lattice structures

Five lattice cell designs are shown in Fig. 2. Auxetic lattices are based on rotating square (RS) and re-entrant (RE) shapes, respectively. Re-entrant cells with different sizes are denoted as Re-Entrant-Small (RE-S) and Re-Entrant-Large (RE-L). The dimensions of two non-auxetic shapes, i.e., rectangular (RT) and honeycomb (HC), are designed to ensure comparable volumes of lattice bending reinforcements to RE-S and RE-L, respectively. Among all lattice designs, only RS has a three-dimensional configuration. This 3D geometry is constructed by first placing two planar rotating square layers in parallel at a certain distance, then connecting them with vertical struts, and finally rotating the assembly by 45° around the central axis. The detailed design process was illustrated in Meng et al. [20]. The 3D RS structure exhibits auxetic behavior in both in-plane and out-of-plane directions, distinguishing it from the other lattices, which are composed of planar geometries connected by horizontal struts. As a result, the deformation of these other lattices occurs primarily within the plane, while RS enables multidirectional expansion and contraction.

Lattice structures were printed with vat photopolymerization (VPP) approach, which features high resolution and ability to create complex 3D structures. High-elongation resin (Loctite 3D IND405 HDT50) was adopted as raw printing material, the physical properties of which are summarized in Table 1.

3D models of lattice structures were first fed into slicing software to convert the 3D structure into horizontal layers with prescribed parameters. During manufacturing, the 3D printer (ELEGOO Mars 3) solidifies the photopolymer resin by exposing it to ultraviolet light in the prescribed area. After printing of each layer, solidified layers were vertically pulled out of the liquid resin to allow for successive solidification of the next horizontal layer. The printing parameters are summarized in Table 2. The layer exposure time represents the time each layer is exposed to UV light, which is longer for bottom layers to ensure better adhesion to the building plate. The light-off delay is the time gap between two successive layers' exposure. After removal, the printed lattice structures were cured for 5 min with 405 nm UV light.

2.2. Uniaxial tensile tests of lattice structures

To gain a better understanding of lattice reinforcements' tensile behavior, dog-bone samples were printed for uniaxial tensile tests. Given that the lattice reinforcements were fabricated using VPP approach, which enables fairly uniform curing of photopolymer resin under ultraviolet light, the printed parts exhibit negligible anisotropy [20]. As illustrated in Fig. 3, the clamping ends of the sample are solid, while the gauge region are lattice structures with dimensions of 16 mm × 72 mm × 7 mm. The specimen dimensions were determined with reference to ASTM D638-22 standard [57] for tensile testing of plastic materials and subsequently adjusted to accommodate the arrangement of lattice cells, ensuring a representative and stable mechanical response. All samples were printed vertically as shown in Fig. 3.

The loading setup is shown in Fig. 3. Specimens were uniaxially loaded at a fixed loading rate of 0.4 mm/min by the SCHENCK TREBEL machine whilst two linear variable displacement transducers (LVDTs)

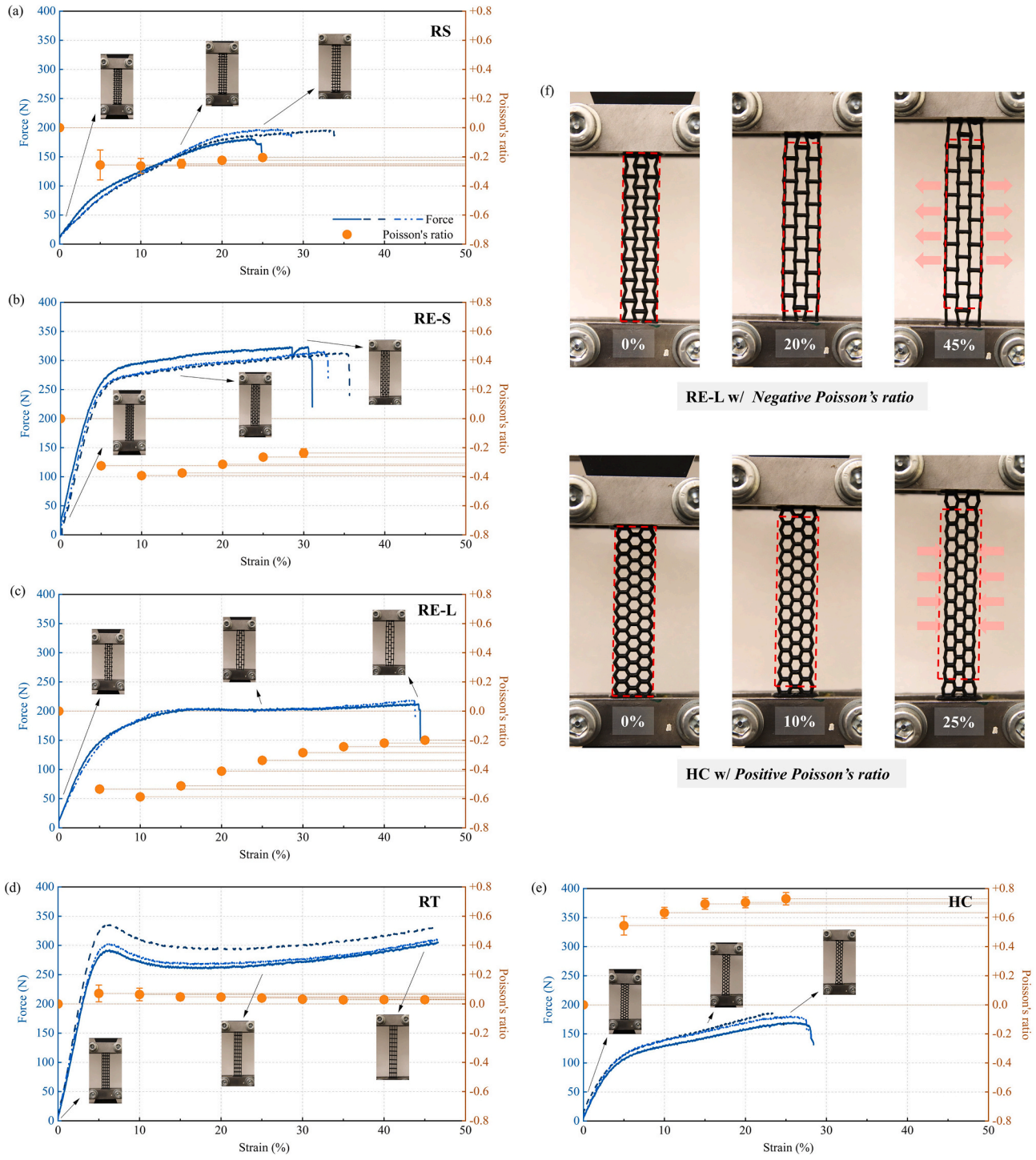

Fig. 6. (a-e) Tensile properties and Poisson's ratios of lattice structures, and (f) close-up images of RE-L and HC's lateral deformation at different strain levels.

measured the average tensile strain in the gauge region. The lateral expansion/contraction was recorded and measured by image analysis.

2.3. Four-point bending tests of LRCCs

The dimensions of LRCC specimens were 160 mm in length, 40 mm in width, and 40 mm in depth. Five types of lattice reinforcements were printed for the preparation of LRCC samples (see Fig. 4(a)). The outline geometries of the reinforcements are approximately 16 mm × 16 mm × 120 mm. Slight deviation may exist due to the arrangement of different lattice cells. Before mortar casting, printed lattice reinforcement was glued to the lower half of a foam mold to properly position the reinforcement (Fig. 4(b)). The location of the reinforcement is schematically shown in Fig. 5(c).

For cementitious matrix, the binders used include ordinary Portland cement (CEM I 42.5 N) and fly ash. Silica sand (0.125–0.250 mm) was adopted as fine aggregate. Rheology of the mortar was tailored by using a superplasticizer (Glenium 51). The mix proportions are shown in Table 3. The water-to-binder ratio and sand-to-binder ratio were 0.40 and 0.46, respectively. The mortar mix design used in this study was selected to ensure sufficient flowability for complete infiltration of the 3D lattice reinforcements, while also providing mechanical

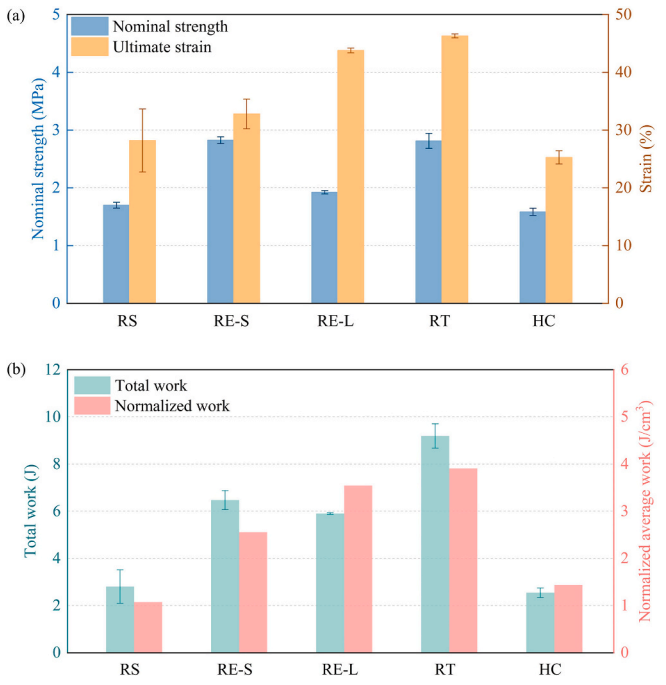

Fig. 7. Tensile properties of lattice structures. Nominal strength in (a) is calculated by dividing force by nominal cross-sectional area (16 mm × 7 mm). Normalized work in (b) are specific energy absorption normalized by the solid volume of lattice structure.

compatibility with the lattice structures. In addition, this mix design remains consistent with that in previous studies [12,20,44]. During mixing, all dry ingredients were pre-mixed for 2 min. Water and superplasticizer were added afterwards, and the mixing continued for another 4 min. After casting, the samples were vibrated for 30 s. LRCC samples were demolded after 48 h and cured for another 26 days under a temperature of 20 ± 2 °C and a humidity of 96 ± 2 %.

The setups for four-point bending tests (Fig. 5) consists of two main parts: (1) loading setup, and (2) acoustic emission test (AET) system. The tests were carried out on a UTM-25 machine, as shown in Fig. 5(b). The loading and supporting spans were 50 mm and 120 mm, respectively (Fig. 5(c)). Loading rate was kept at 0.5 mm/min. Two acoustic sensors (Wideband Differential (WD) AE Sensor with an operating frequency range of 100–900 kHz) were attached to the front and top surfaces of the composite sample to detect acoustic signals resulting from sample damage. The acoustic data were recorded by a Micro-II Express AE Chassis (Mistras Group, Inc) and analyzed with MATLAB.

To better comprehend the interaction between reinforcement and matrix, micro computed tomography (CT) scanning was conducted to capture the interior morphology of fractured samples. In four-point bending tests, LRCC samples were loaded to complete failure. Half samples were collected for scanning with a Phoenix X-ray Nanotom μ-CT scanner. Scanning started from the fracture plane to the undamaged end. The slicing interval of CT scanning was 20 μm, indicating the thickness of a reconstructed voxel is 20 μm. By combining the sliced images, the interfacial fracture between lattice reinforcement and mortar matrix was visualized in the software Dragonfly.

3. Results and discussions

3.1. Tensile properties of lattice structures

The force-strain relationship and Poisson's ratio evolution of different lattice structures are shown in Fig. 6. The five groups exhibited distinct mechanical response patterns, yet consistently demonstrated the lattice structure's remarkable ductility and energy absorption capacity under tension.

Among auxetic groups, RS showed a different tensile response with RE groups. The force-strain curve of RS was characterized by a gradual decline in stiffness until struts began to fail and led to a loss of overall load-bearing capacity (Fig. 6(a)). The average ultimate tensile strain was below 30 %. In contrast, the curves for RE-S (Fig. 6(b)) and RE-L (Fig. 6 (c)) exhibited bilinear profiles. Following the initial linear elastic region, stiffness progressively decreased, transitioning into a yield plateau at 5 %−10 % tensile strain.

In terms of lattice size, RE-L demonstrated lower load-bearing capacity and stiffness compared to RE-S (Fig. 7(a)). This is attributed to the sparser arrangement and reduced number of struts in the cross-section of RE-L despite the identical strut diameter. Nevertheless, the larger lattice size provides greater vertical deformation space, allowing RE-L to reach an ultimate tensile strain of 43 %, compared to 32 % for RE-S. This enhanced deformation capability resulted in a 39 % higher unit energy absorption capacity for RE-L than that of RE-S, when normalized by the solid volume of the lattices (Fig. 7(b)).

For non-auxetic lattices, RT and HC possessed notably different mechanical behaviors. HC showed a bilinear tensile response; nonetheless, the tensile response of RT resembles the yielding behavior observed in metals: following the linear elastic phase, yielding emerged, after which the load decreased slightly before transitioning into a gradually ascending plateau. The experiment was terminated when the tensile strain reached 45 % due to the travel limit of the testing apparatus. At this point, the cross-sectional area of the axial struts in RT had decreased, similar to "necking" in metal, with no fractures observed.

The above experimental observations revealed that the tensile performance of lattice structures is primarily influenced by following key factors:

(1) *Structural dimensionality,* i.e., *plane-dominant* vs. *3D-dominant designs.* Among the five lattice configurations examined, the RS structure, derived from a rotated plane-dominant design, inherently exhibits a three-dimensional spatial form. This unique configuration provides RS with greater freedom of deformation and enhanced flexibility. Consequently, RS demonstrates the lowest stiffness and lacks a distinct yielding point.

(2) *Alignment of lattice struts with the load direction, particularly the presence of angled struts.* Angled or curved struts, such as those in RE, RS and HC geometries, are commonly seen in lattice structures to facilitate and augment lattice deformation. However, misalignment between the axial force in individual struts and the overall load direction can lead to stress concentrations, particularly at corners and joints. In this study, tearing of angled struts was identified as a critical failure mode in RS, RE, and HC groups (see Fig. 8(a) and Fig. 8(b)). In contrast, RT yielded a different response. Although it shares the same number of cells and equivalent solid cross-sectional area as RE-S, the axial direction of RT's longitudinal struts is perfectly aligned with the tensile load, leading to more efficient load transferring and less stress concentrations at the "armpit" locations. As a result, no strut fractures were observed in RT even at a tensile strain of 45 % (Fig. 8(c)), and RT showed an absolute advantage regarding mechanical properties.

(3) *Lattice cell size.* Lattices with smaller cell sizes, such as RE-S, featured higher cell density and a larger effective cross-sectional bearing area compared to larger lattices like RE-L. Consequently, RE-S exhibited higher stiffness and nominal strength than RE-L (Fig. 7(a)). However, the larger lattice size of RE-L allowed for greater axial deformation before struts fractured, resulting in a higher ultimate tensile strain and more efficient energy absorption than RE-S.

For dog-bone samples examined in this study, all three auxetic designs exhibited a pronounced negative Poisson's ratio. The maximum

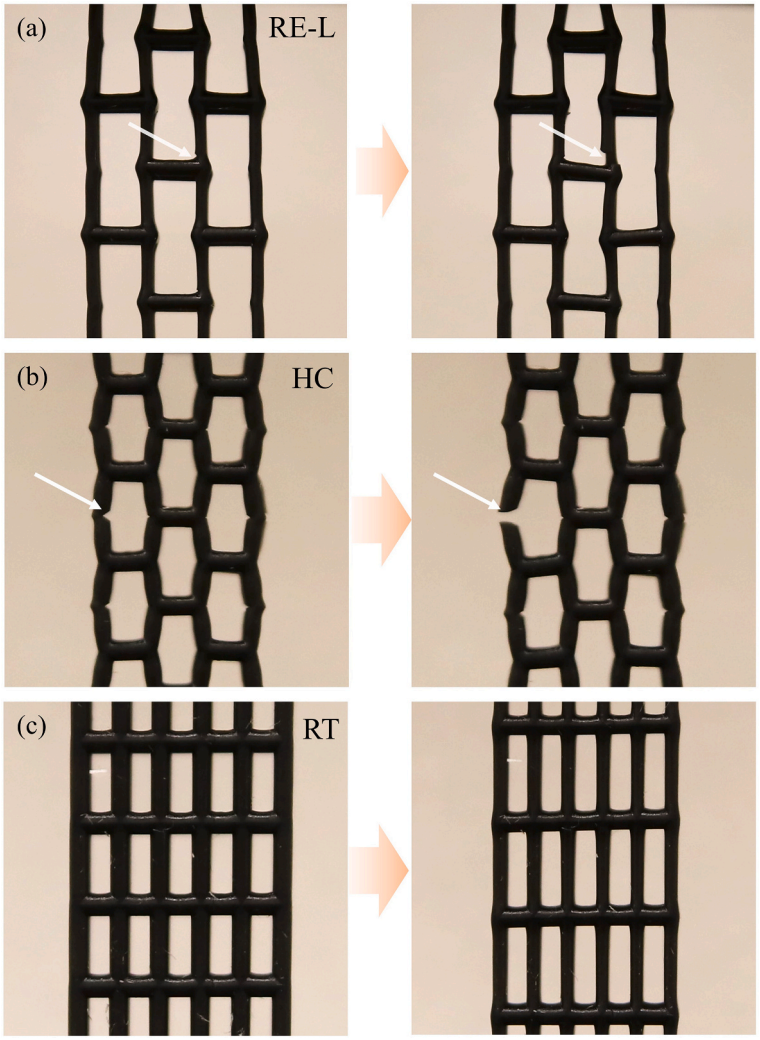

Fig. 8. Close-up images of strut behavior. Left and right images of (a) and (b) show sample status before and after strut breakage, respectively. The left image of (c) is a virgin RT sample, while the right one is at 45% tensile strain.

negative Poisson's ratio occurred at approximately 10 % longitudinal strain for all configurations. Among them, the RE lattices demonstrated larger lateral expansion than RS. Further, the reduced lattice density in RE-L led to a larger allowance for axial stretching and lateral expansion. Consequently, RE-L reached a maximum negative Poisson's ratio of −0.6.

For non-auxetic designs, HC reached a positive Poisson's ratio of +0.7 at maximum, which increased with longitudinal axial strain until failure. This indicates HC's exceptional deformation capacity. In contrast, RT experienced significant longitudinal elongation with minimal lateral deformation, resulting in an nearly zero Poisson's ratio. It should be noted that, nonetheless, the Poisson's ratios of the above lattice designs may be affected by the bulk geometries of the tested samples.

3.2. Flexural properties of composites

3.2.1. Mechanical performance

Fig. 9 presents the results of the four-point bending tests for LRCCs, revealing consistent mechanical response patterns across different reinforcement designs. All LRCCs exhibited a two-stage mechanical behavior: the brittle fracture of the cementitious matrix, followed by the post-peak response dominated by the LR and its interaction with the matrix.

The initial phase displays consistency across all groups, as the development of the first crack in the mortar is not strongly affected by the presence of the lattice reinforcement, considering their minor volume fraction. However, once the crack opens, stress is redistributed to the LR's struts near the cracking plane. The bearing capacity and deformation ability of LR in this region become critical to the composite's post-peak performance in the second phase.

For instance, there was no substantial stress growth in RS-LRCC during the second phase. As established in previous sections, the struts failed to provide continuous load-bearing enhancement after stress redistribution. This led to rapid failure of the composite and resulted in deflection softening. In contrast, the RT-reinforced LRCC demonstrated a pseudo-deflection hardening behavior. The successive fracture of struts was accompanied by a load increase, surpassing the initial matrix cracking load. This is attributed to the excellent ductility and tensile performance of the RT lattice structure in the longitudinal direction. The superior elongation capacity of RT led to the excellent performance of the composite (see Fig. 10), e.g., an energy absorption capacity up to 23 times that of the reference mortar. This makes the RT-reinforced composite highly attractive for energy-dissipation structural applications, particularly given the relatively low reinforcement ratio in this study — 3.5 % for RT-LRCC — compared to previous literature. In addition, the RE-S, RE-L and HC-reinforced LRCCs also demonstrated enhanced energy absorption, i.e., 5–6 times compared to the control group.

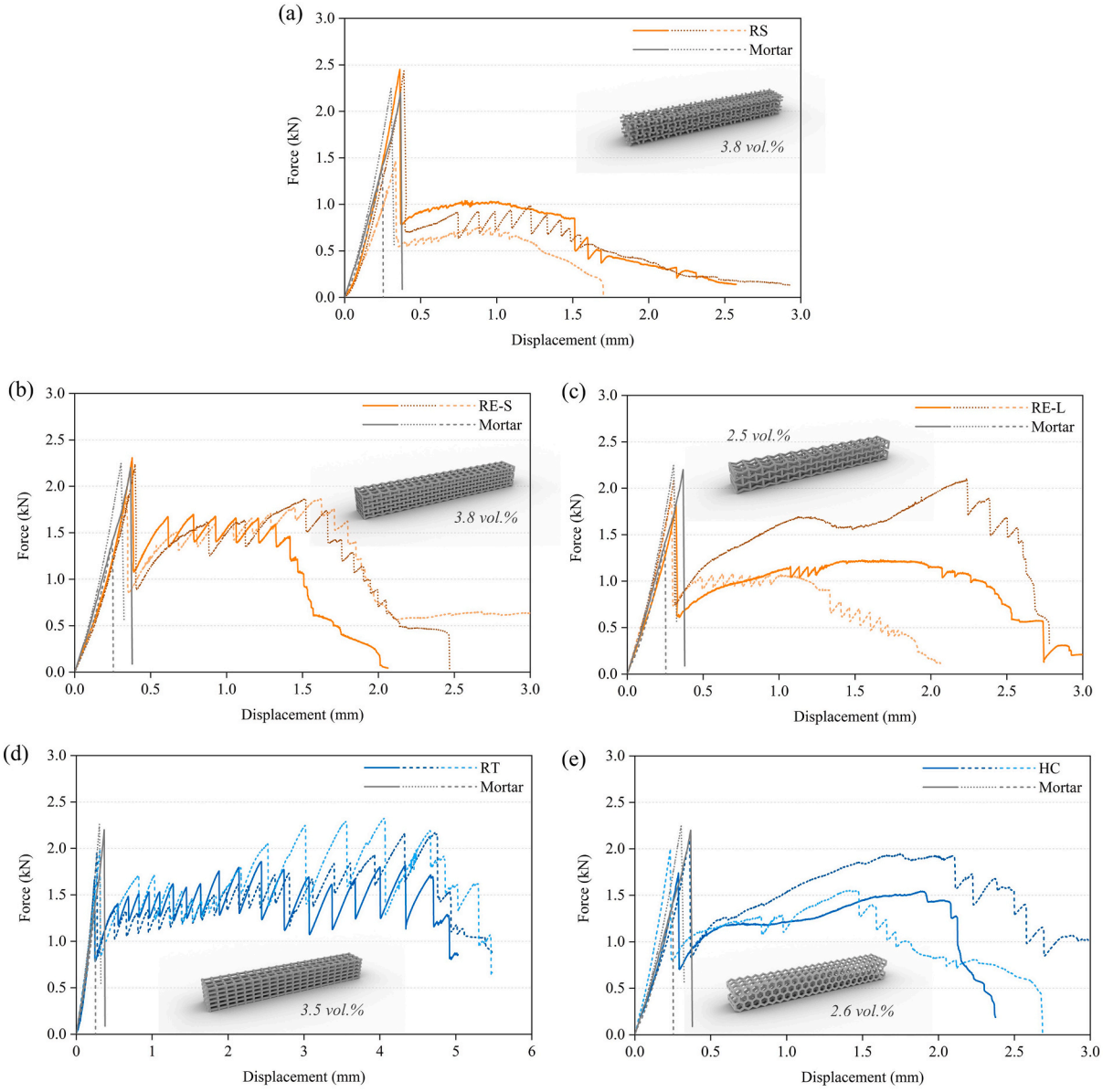

Fig. 9. Force-displacement relationships of LRCCs and reference mortar. Volume percentage noted in the figures represents the reinforcing ratio of each group.

In the composite behavior analysis, two comparable pairs can be identified considering the lattice design, cell size, and reinforcement volume: RE-S vs. RT, and RE-L vs. HC. RS is excluded from this comparison due to its unique spatial structure.

RE-S and RT share similarities in reinforcement ratio and lattice arrangement. However, the contrasting lattice configurations result in vastly different mechanical behaviors in the composites. RT-LRCC exhibited an ultimate failure strength that is 136 % of RE-S-LRCC and absorbs 3.5 times more energy. The key factors contributing to these differences are:

(1) *Diverging deformation capacities of lattice structures.* As seen in Fig. 9(b) and (d), the mechanical responses of the two remained similar before 1.5 mm displacement. At this displacement level, the crack opening in RE-S-LRCC approached the maximum deformation capacity of local lattice cells. Once the lowest struts began to fracture, the redistributed tension was quickly transferred to upper struts, resulting in successive strut failures and global collapse. In contrast, RT's deformation capacity was not exhausted at the similar crack opening, enabling RT to continue flexural hardening.

(2) *Difference in Poisson's ratio.* The auxetic nature of RE lattice caused lateral expansion of the LR near the crack surface, resulting in mechanical interlocking with the matrix and preventing debonding. This limited RE's capacity for further deformation. Conversely, the nearly zero Poisson's ratio of RT facilitated debonding and local pullout of the lattice, allowing for greater deformation.

These differences are further evidenced by Fig. 11. CT scanning of fractured LRCC specimens reveals the cracks and voids area surrounding the fracture surface. Note that the figures reconstructed from CT scanning only show the region within 10 mm depth from the cracking plane. Fig. 11(a) shows a close-up of the crack in RE-S before complete composite failure, where only minor pullout of the LR was visible. The distribution of voids in the colored area in Fig. 11(b) highlighted the occurrence of debonding around the bottom unit of the reinforcement, displaying the approximate contour of RE-S. Nonetheless, no significant

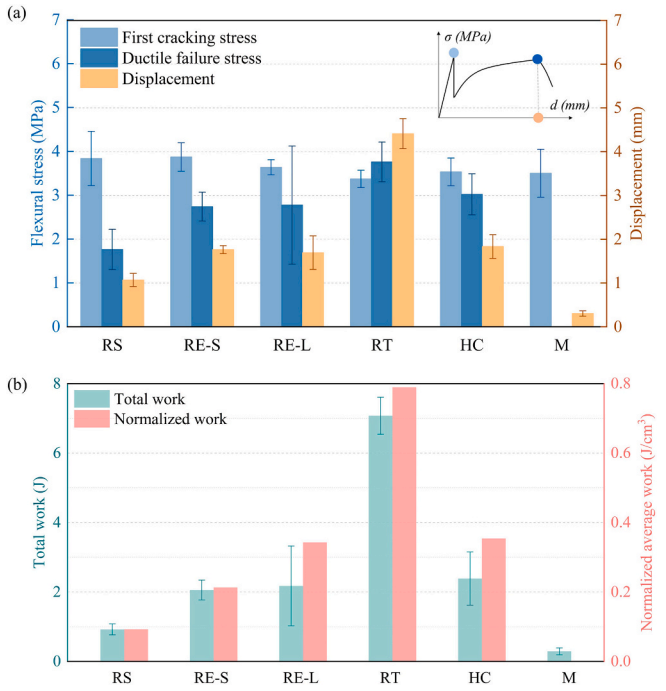

Fig. 10. (a) Mechanical properties and (b) energy absorption abilities of LRCCs and reference mortar. Normalized work in (b) are specific energy absorption normalized by the solid volume of lattice reinforcement.

debonding was observed in the upper portion of the LR. In contrast, RT in Fig. 11(c) showed substantial pullout, and the corresponding CT image in Fig. 11(d) revealed circumferential debonding, forming a connected channel around the LR. Furthermore, the scale of debonding in RT was considerably larger than in RE-S. This sharp contrast evidenced the differences in their interfacial behavior and interaction with matrix.

Additionally, the experimental results indicate that RT-LRCC was the only group to exhibit a clear pseudo flexural-hardening behavior due to the abovementioned reasons, while the other groups showed relatively limited improvement. Achieving comparable performance in other designs requires careful tuning of both the matrix and reinforcement properties. For example, reducing the matrix stiffness can alleviate abrupt load transfer during cracking, while employing tougher or stiffer reinforcement materials may improve structural integrity and better align with the matrix behavior. In all cases, the key lies in optimizing the synergy between the reinforcement and the matrix. Future optimization efforts could focus on improving the reinforcement strength and tuning matrix properties to better accommodate stress redistribution and delay failure, thereby enabling flexural hardening behavior across a broader range of lattice designs.

The second pair, RE-L and HC, possesses similar reinforcement ratio, lattice arrangement, and mechanical performance. The similarity in their macroscopic performance offers an ideal basis for examining the underlying differences in failure mechanisms. These distinctions, which are primarily driven by the unique forms of the lattice design, will be identified and detailed in Subsection 3.2.2.

In addition, an intriguing finding in this test is that the RE-S-LRCC did not outperform the RE-L-LRCC as expected. This suggests that a higher lattice density does not necessarily translate to improved composite performance, even though it enhances the tensile stiffness and strength of the lattice structure itself. The composite's behavior is primarily governed by the local lattice structure near the crack plane, rather than the overall behavior of the whole LR. Due to the bonding and mechanical interlocking between the reinforcement and the matrix, the part of reinforcement positioned far from the fracture surface contributed minimally to the overall flexural response; while the portion of the lattice that did engage in stress transfer was closely tied to the crack opening and its intrinsic deformation capacity. In the case of RE-S, although the lattice demonstrated greater stiffness and strength than RE-L, its deformation capability was limited. Furthermore, the failure in both groups was primarily driven by strut tearing at joints. Both factors led to the premature strut failure of RE-S and inferior post-peak ductility. Therefore, it should be highlighted that performance-driven design is essential in LRCC structures – through precise tuning and design, the composite performance can be optimized while minimizing the amount of reinforcement used.

Further, the current study distinguishes itself from existing research on auxetic-reinforced composites. Rosewitz et al. [51] embedded auxetic lattices in a similar orientation to the present study; however, the resulting composites did not exhibit clear post-peak behavior. In [49], planar auxetic lattice was used to reinforce pre-notched beams, where the post-cracking strength was less than 50 % of the initial cracking strength. Strain-hardening behavior in thin-plate composites was reported by [25], though the reinforcement had a notably large volume fraction. In contrast, the specimens in this study retained more than 70 % of their peak strength after initial cracking, along with multiple cracking patterns. These results suggest a distinct reinforcing mechanism in the current study. While direct quantitative comparisons are limited by differences in lattice geometry, reinforcement volume, and boundary conditions, the current findings provide complementary insights into the use of lattice reinforcements for enhancing ductility in brittle matrices.

3.2.2. *Acoustic emission analysis*

3.2.2.1. *Damage evolution based on accumulated AE events and AE rate.*

Acoustic emission test was employed in this study to investigate the fracture mechanisms of different LRCCs during four-point bending tests. Each effective acoustic emission (AE) signal is recorded when it surpasses a predefined threshold, signifying a significant energy release within the sample. Each AE event corresponds to distinct occurrences such as crack initiation, crack propagation, debonding, or reinforcement breakage. Signals can be characterized, distinguished and classified by various parameters, which translate the acoustic emission signals into useful information about material fracture and matrix-reinforcement interaction. The fundamental acoustic emission parameters are illustrated in Fig. 12, reproduced from [58] under the terms of the Creative Commons CC BY license.

Fig. 13 shows the accumulated AE events (AAE), event rate, and load development over time for representative LRCCs. AAE tracks the total number of event signals collected from the start of loading (time zero), while AE event rate measures the number of AE hits per unit time. By analyzing these two parameters in conjunction with the load-time curve, three common phases can be identified in LRCC's flexural response:

(1) *Microcrack Initiation.* This phase corresponds to the elastic region of the load curve until the initial matrix crack. During this phase, AAE curves show a slow and steady increase, as only limited microcracking occurs in the matrix. A relatively small number of acoustic emission signals are recorded. Similarly, the AE event rate remains minimal.
(2) *Crack Propagation.* This critical phase starts at a key point where the macro-crack initiates and propagates. The load sharply decreases by 50 %–70 % as the cementitious matrix fractures and loses tensile capacity. In AAE curve, a notable transition point in the slope is observed, as shown in Fig. 13(a). The slope notably increases after this point, reflecting the rapid accumulation of AE events. A small burst in AE event rate, which correlates to the macroscopic cracks propagation, is also present. Further in this phase, tensile load is transferred to LR, leading to successive

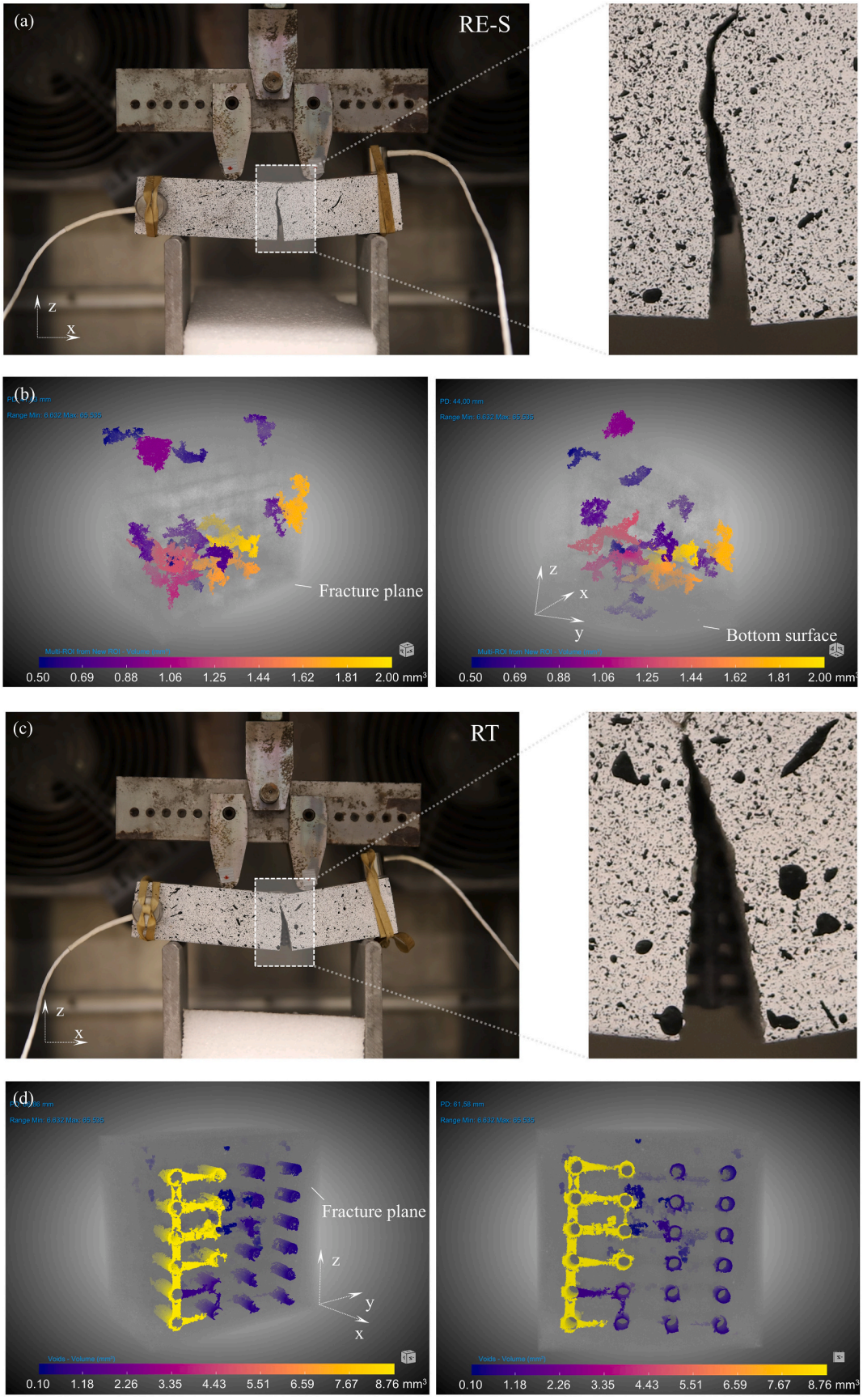

Fig. 11. Close-up images and reconstructed CT scanning images of (a-b) RE-S-LRCC and (c-d) RT-LRCC. The colored area represents voids and cracks. Color legends represent the void volume (unit: mm^3).

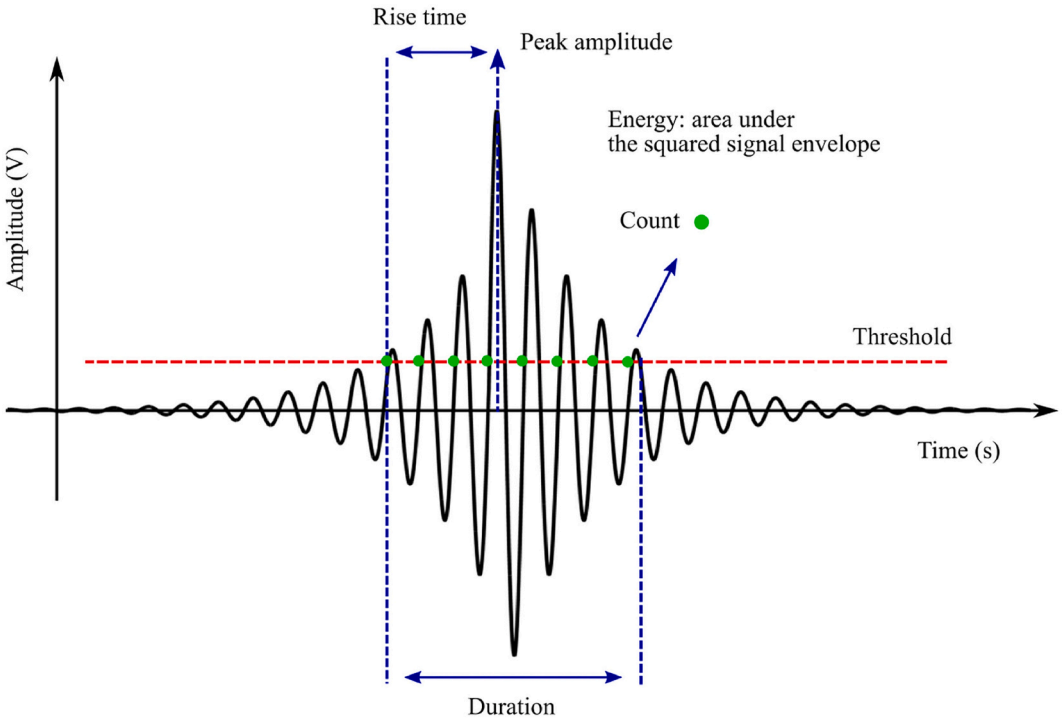

Fig. 12. Acoustic emission parameters. Reproduced from [58] under the terms of the Creative Commons CC BY license.

fractures of struts. The acoustic emission signals captured at this time reflect both matrix crack growth and LR strut fractures. Throughout this stage, AAE shows a steady linear increase, and AE event rate stabilizes around the post-peak stress plateau, extending until the composite reaches its ultimate failure.

(3) *Accelerated Damage/Ultimate Failure.* The third stage usually follows the secondary load peak, where the AE event rate shows sharp spikes and AAE curve steepens, indicating rapid damage accumulation. This typical stage is illustrated in Fig. 13(b), and applies to RE-S-LRCC, RE-L-LRCC and HC-LRCC groups.

Nevertheless, RS and RT groups showed different patterns other than the typical phase. RS-LRCC quickly entered the softening stage once the matrix's tensile strength was exhausted. As a result, RS-LRCC did not exhibit a distinct third stage but rather continued the second stage until complete failure. In contrast, for RT- LRCC, a substantial increase in AE event rate and AAE occurred around the 300 s mark, signifying accelerated damage, although the capacity of the sample was not yet exhausted. It should be noted that the AE signals collected during this period correspond not only to crack openings and LR fractures but also include a large number of mode II shear cracks, as will be further discussed in the following section.

3.2.2.2. Damage type classification based on AF-RA and peak frequency analysis. To better prehend the underlying damage mechanism in LRCCs, AF (Average Frequency)-RA analysis was performed to distinguish different types of microscopic fracture phenomena. Specifically, AF is defined as the ratio of counts number to signal duration. A high AF value signifies a rapid rate of threshold crossings within a short duration, producing sharp, high-frequency signals. RA represents the ratio of rise time to peak amplitude, reflecting the event's development rate. A high RA value typically suggests slower crack propagation. Owing to the mutual analysis of AF and RA, it is possible to classify crack types. It is generally recognized that high AF and low RA correspond to tensile cracks (Mode I), whereas low AF and high RA are more representative of shear cracks (Mode II), which are often linked to interfacial debonding or frictional sliding [59–62].

AF-RA plots for each group of LRCCs were created (see Fig. 14). The acoustic emission signals are represented by discrete data points, classified according to the time period in which they occur. The normal distribution curves shown above and to the right of each figure further highlight the migration of data clusters along both the RA and AF axes. As loading progresses over time, the cluster of points gradually shifts from the upper-left corner toward the lower-right. Initially, the failure mode is characterized by high-frequency, rapid, and sharp tensile crack openings, which gradually transitions to larger-scale, slower but sustained shear failure and crack surface friction. The shift from tensile to shear crack dominance aligns well with experimental observations, where the post-matrix-cracking failure is primarily controlled by the LR behavior and the interaction between the LR and matrix.

During the initial 0–50 s interval, the AE signals are predominantly characterized by high AF and low RA, corresponding to the formation of microcracks and the sudden opening of matrix cracks in the early stage, i.e., the cracks are primarily tensile-dominant. Therefore, signal recorded during the 0–50 s interval from all groups were plotted together to determine a dividing line (dash line in the figure). It is ensured that more than 90 % of signals fall above the line, indicative of tensile cracks, while the points located on the lower-right side are classified as shear-related cracks [63]. For each group of LRCC, the proportion of signals that fall on either side of the dividing line was recorded and illustrated in the pie charts. It should be noted that the data included in these pie charts only account for the period before ultimate failure to ensure a fair comparison and eliminate the influence of catastrophic failure events that could skew the analysis.

The number of collected AE signals in RS-LRCC showed a significant reduction after 50 s, and shear-dominant cracks accounted for merely 18.8 % of the total AE signals. This is because the early fracture of RS reinforcement occurred before interface debonding or sliding could take place, leading to the global failure of the composite before more complex shear mechanisms were activated.

For RE-S and RT reinforced LRCCs, the number and proportion of shear-dominant cracks increased significantly compared to RS-LRCC. RT-LRCC showed 38.2 % of shear-dominant cracking, the largest among all the groups, due to the partial pullout of RT observed near the

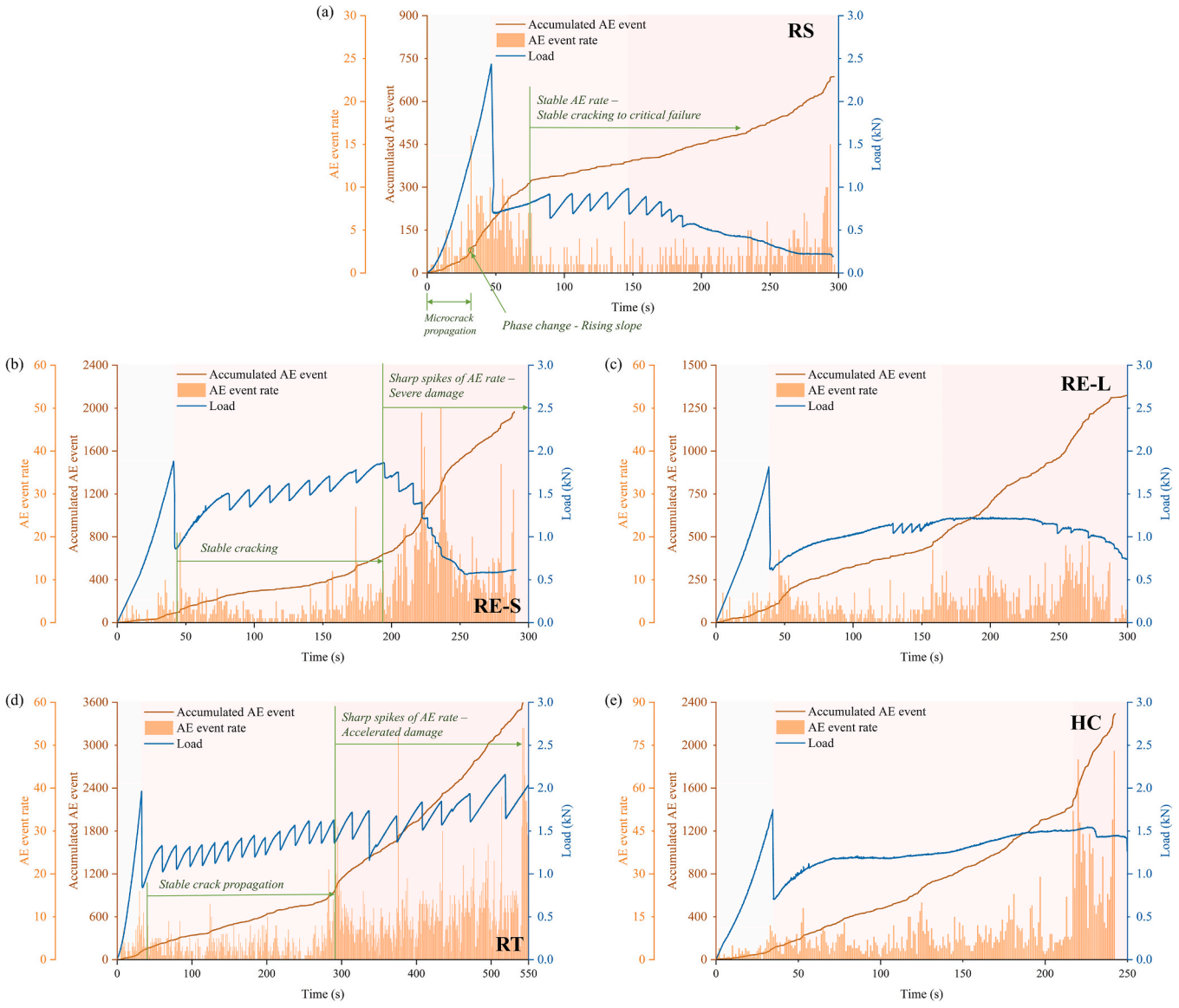

Fig. 13. Accumulated AE event and AE event rate in the time domain for LRCC samples under four-point bending.

fracture surface, as seen in Fig. 11(c). AE signals generated by the interfacial debonding and friction between LR and the matrix were highlighted. Meanwhile, RE-S has relatively fewer shear-dominant cracks due to the lower debonding level, as discussed in the previous section.

A more effective comparison can be made between RE-L and HC. According to Fig. 14(c) and Fig. 14(e), the auxetic RE-L reinforced composite demonstrated a lower percentage of shear cracks compared to the non-auxetic HC, indicating reduced instances of debonding and frictional sliding.

Furthermore, the analysis of peak frequency (PF), presented in Fig. 15, shows significant differences between the two composites. PF represents the frequency at which the acoustic emission signal reaches its maximum amplitude within its frequency spectrum, different from previous analyses which are based on the time spectrum. In addition to AF-RA, PF can also be a useful indicator for different microscopic damage types in solids [64–66]. In the post-peak phase (after 50 s), the ratio of low-frequency signals to high-frequency signals in RE-L-LRCC was substantially lower than that in HC-LRCC, indicating that auxetic RE-L reinforced composite possessed a smaller proportion of low-frequency, mild shear cracks [67]. This trend aligns with the earlier AF-RA analysis results, further validating the conjecture that, despite their comparable mechanical properties, auxetic and non-auxetic reinforcements exhibit different reinforcing mechanisms. The auxetic reinforcement can expand near the crack surface once a crack initiates, which effectively inhibits interfacial debonding. FEM simulation in Section 4 further validated this finding.

4. Numerical modeling

Complementary to the experimental analyses, Finite Element Method (FEM) simulations were performed to gain more insight into the deformation mechanism of the reinforcement in relation to the composite behavior of the LRCCs. The commercially available FEM software ABAQUS/Explicit was employed to simulate the uniaxial tensile and four-point bending tests of the RE-S design. The damage evolution of the cementitious matrix was incorporated by means of the commonly used Concrete Damaged Plasticity Model (CDPM), as described and used throughout previous studies of the authors [12,35,44,68]. The 3D-printed high-elongation resin was implemented through a plastic material model in combination with the ductile damage initiation criterion, which allowed for dictating the material degradation at the onset of

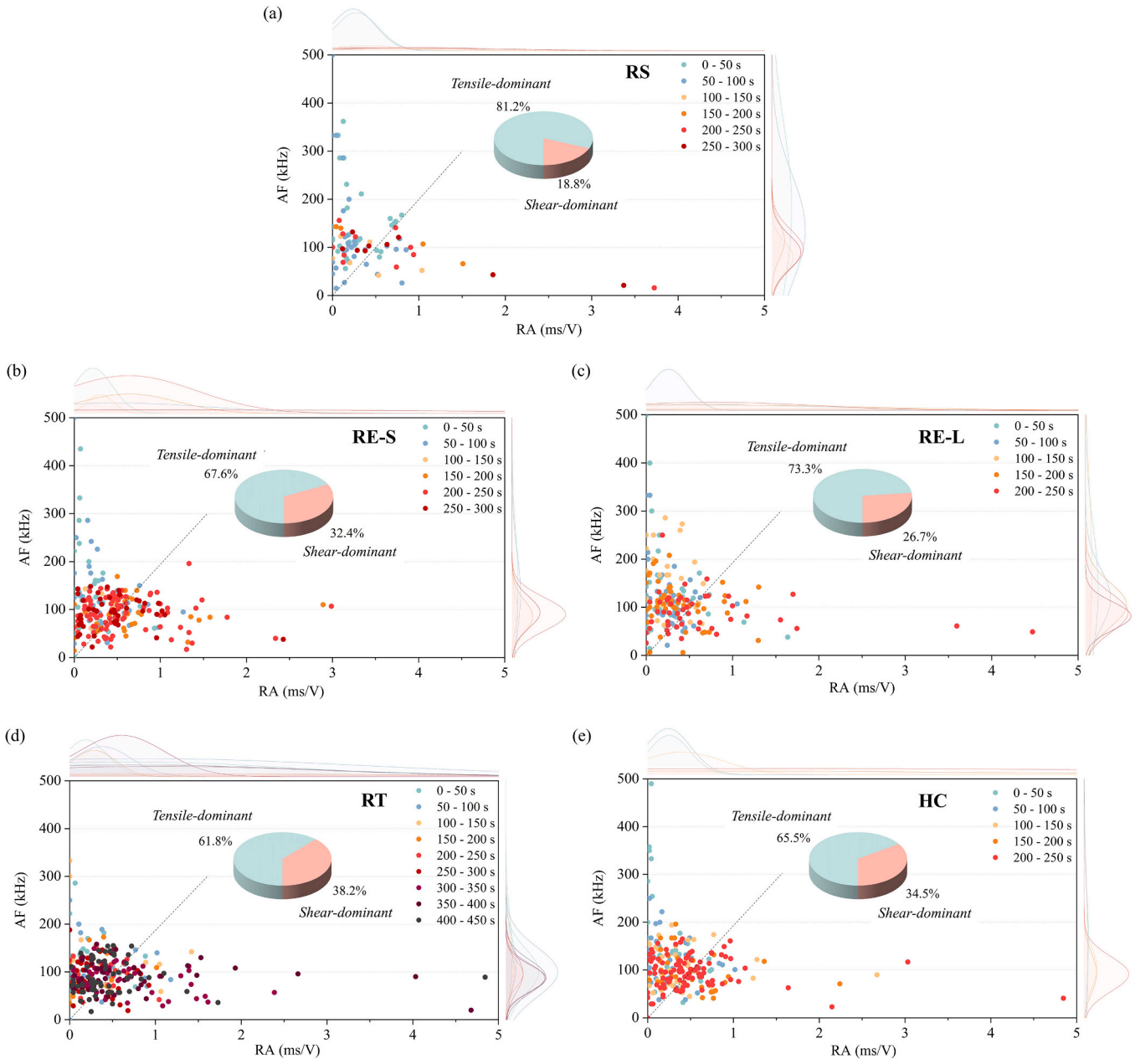

Fig. 14. Correlation between RA and AF. Pie charts show the signal count proportion above and below the dividing line, which signifies crack classification.

damage. In all simulations, element deletion was activated to explicitly capture the fracture mechanisms.

4.1. Model calibration

The input for the plastic material model was determined by converting the engineering stress–strain curve of RE-S lattices (derived from Fig. 6(b)) into a true stress–strain curve, where Young's modulus, yield stress, and ultimate stress were obtained. A true stress-plastic strain graph was subsequently constructed to determine the fracture strain. Finally, the resin was modeled with a density of 1.15×10^{-9} t/mm^3, a Young's modulus of 325 MPa, a Poisson's ratio of 0.2 and a fracture strain of 0.8. Table A1 includes the input parameters for the plastic material model.

To verify the input parameters, a model replicating the RE-S tensile experiment was simulated. It was found that the simulated force-strain curve agrees well with the experimental observations, following the same initial linear elastic trajectory and subsequent stiffness deterioration, as shown in Fig. 16. Moreover, the simulation's nominal strength, ultimate strain, total work and normalized work correlate well with the experiments, with deviations less than ±10 %.

Accounting for the trade-off between computational demand and accuracy, as well as adequately discretizing the architected lattice structure, 4-node linear tetrahedron elements (C3D4) with an average mesh size of 0.5 mm were selected throughout all models. For the cementitious mortar, uniaxial tensile and compression simulations were used to calibrate the CDPM input according to the procedure described in Ref. [44] for the same mix proportions. This involved numerical tensile tests on a dog-bone cementitious sample with the same mesh size as the composite model. Similarly, a digital cubic specimen was compressed between two loading plates assigned with a friction coefficient of 0.1. In the end, the matrix was modeled with a density of 1.87×10^{-9} t/mm^3, a Young's modulus of 1010.5 MPa and a Poisson's ratio of 0.2. The CDPM input for plasticity, compressive behavior and tensile

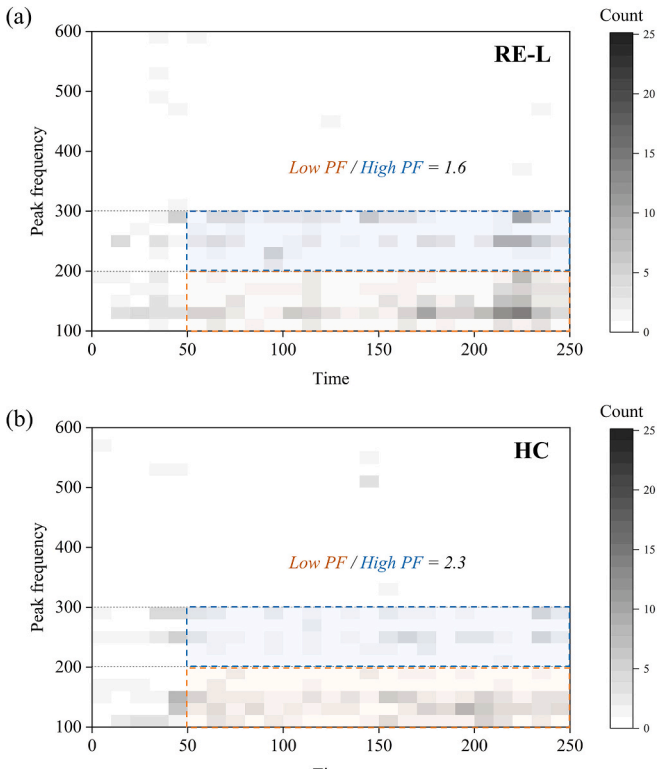

Fig. 15. Peak frequency analysis for (a) RE-L-LRCC and (b) HC-LRCC.

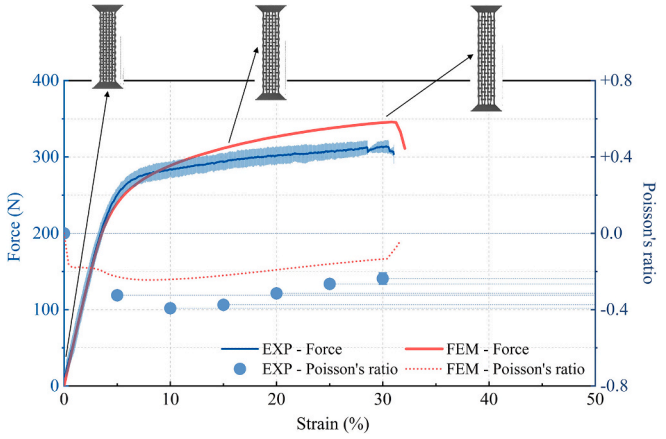

Fig. 16. Comparison of experimental (EXP) and numerical (FEM) tensile properties and Poisson's ratio of RE-S LR. The shaded area represents the standard deviation of EXP force.

Table 4
CDPM input for plasticity.

Dilatation angle	Eccentricity	f_{b0}/f_{c0}	K	Viscosity parameter
35	0.1	1.16	0.667	0.001

behavior are summarized in Tables 4, 5 and 6, respectively.

4.2. Simulation results

Four-point bending simulations of the RE-S-LRCC were carried out. One-half of the specimens were simulated by applying symmetrical boundary conditions along the longitudinal axes. Load and support conditions at the upper and lower faces of the samples were facilitated through four rigid rollers (R3D4 elements with an average mesh size of 0.25 mm). The roller-mortar interaction properties concerned a friction coefficient of 0.1 to avoid excessive sliding. A vertical displacement pushing down on the specimens was assigned to the two rollers at the top. All other degrees of freedom were constrained, including the vertical of the bottom rollers. To study the composite behavior between the auxetic deformation mechanism of RE-S and the cementitious matrix, the reinforcement was explicitly modeled by cutting and deleting the architected lattice volume from the cementitious matrix. Similar to previous work on auxetic cementitious composites [12], tie constraint was selected for modeling the interaction between the two materials. Both reference mortar and RE-S-LRCC samples were considered.

Table 5
CDPM input for compressive behavior.

Yield stress (MPa)	Inelastic strain	Damage parameter
12	0	0
22	0.04	0
20	0.16	0.2
9	0.18	0.5
3	0.2	0.7
3	0.4	0.9

Table 6
CDPM input for tensile behavior.

Yield stress (MPa)	Inelastic strain	Damage parameter
3.5	0	0
1	0.014	0.71
0.5	0.019	0.86
0.3	0.025	0.91

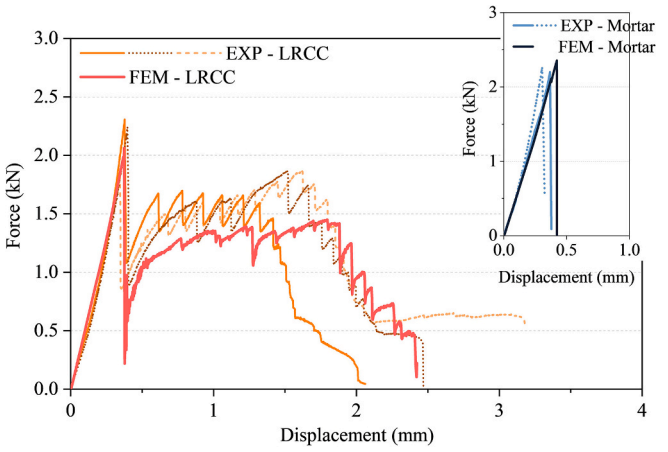

Fig. 17. Comparison of experimental (EXP) and numerical (FEM) force–displacement relationships between RE-S-LRCC and reference mortar.

Fig. 17 shows the similarity in experimental and numerical force–displacement relationships of RE-S-LRCC and reference mortar. In line with experiments, the simulation of LRCC exhibits the same two-stage mechanical response: starting with brittle fracture (i.e., one localized crack), followed by a regain in strength after the peak load. The post-peak plateau can be explained by the deformation and yielding of the LR, while the small load drops related to both the auxetic deformation and the debonding and sliding of LR in the highest stressed region. Near 1.8 mm displacement, the LR reached its stress limit and started to rupture. This was indicated by the stair stepping downwards in Fig. 17. Furthermore, similar first cracking stress, ductile failure stress, displacement, total work and normalized work are obtained for both the reference mortar and RE-S simulations, as shown in Fig. 18.

The deformed shapes recorded during the simulation are displayed

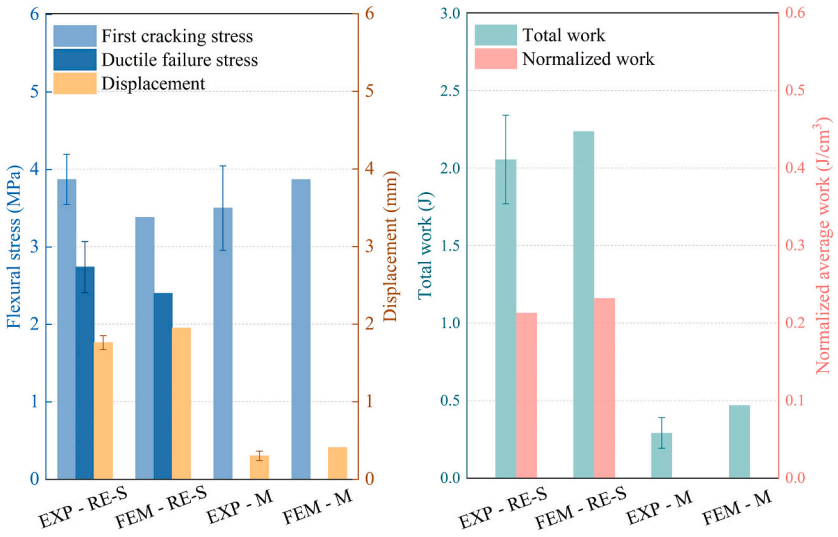

Fig. 18. Comparison of experimental (EXP) and numerical (FEM) (a) mechanical properties and (b) energy absorption abilities between RE-S-LRCC and reference mortar.

on the left of Fig. 19(a), which shows an identical failure mode to the experimental observations. To probe the auxetic deformation mechanism of RE-S in composite behavior, several slightly off-center cross-sections near the fracture surface were taken from the simulation at different deformation levels. The right panel of Fig. 19(a) contains contour plots of the maximal principal stresses in the mortar. The contour colors therein solely indicate negative stresses below − 0.5 MPa, whereas gray indicates higher (mainly tensile) stress values. With increasing deformations, considerable growth in compressive principal stresses can be observed in the plane of the auxetic LR. This is caused by the expansive auxetic deformation mechanism of RE-S induced by the loading, see Fig. 19(b). The simulation thereby proves that auxetic LR provides mechanical anchorage with the mortar and delays debonding.

5. Conclusions and research priorities

The present study sheds light on the tensile response of various lattice reinforcements and their interaction with cementitious matrices at the composite level. The following conclusions can be drawn:

(1) Lattice configuration has a significant impact on the tensile response of lattice structures. Plane-dominant designs (RE, RT, HC) demonstrated remarkable strength and ductility. In this study, the three-dimensional design (RS) exhibited lower stiffness and lacked the yielding plateau due to its inherent geometric characteristics. In addition, increasing lattice density in RE (i.e., reducing cell size) resulted in higher stiffness and load-bearing capacity.
(2) The lateral deformation behavior of auxetic structures was experimentally validated. Furthermore, the influence of lattice unit cell size was evident, as RE-L reached a maximum negative Poisson's ratio of −0.6, highlighting the enhanced lateral expansion with decreased lattice density compared to RE-S.
(3) Lattice reinforcement considerately enhances the deformation ability and energy absorption capability of the composites. With a low reinforcement ratio (2.5 %−3.8 % by volume), the integration of LR improved the energy absorption capacity of cementitious composites to 5 to 23 times that of the reference mortar, showing the effectiveness of lattice reinforcement in enhancing the toughness of LRCC. This characteristic makes LRCC suitable for applications where structural integrity after cracking is critical, such as in protective barriers or components exposed to impact or dynamic loads.
(4) Auxetic and non-auxetic LR exhibited their unique strengths and limitations. Non-auxetic-lattice-reinforced cementitious composites demonstrated excellent energy absorption capacity in specific configurations, e.g., RT-LRCC. However, substantial debonding and pullout were observed near the fracture plane. Auxetic-lattice-reinforced cementitious composites were prone to fracture at corner nodes following stress redistribution after matrix cracking. Nonetheless, the in-plane lateral expansion of auxetic LR inhibited the formation of interface cracks, with debonding primarily confined to the bottom of the tensile zone.
(5) Damage measurement techniques, AET and micro-CT scanning, provided valuable insights into the failure mechanisms of LRCCs, offering complementary perspectives on internal damage. The crack classification derived from AET analysis effectively differentiates the reinforcing mechanisms between auxetic and non-auxetic LRs.
(6) FEM simulations correlated well with the mechanical response and deformation evolution of LR and LRCC. Expansive auxetic deformation of RE-S LR near the composite cracking region was captured, confirming the mechanical engagement with the cementitious matrix provided by the auxetic LR.

Although the present study elucidated the reinforcing mechanism and highlighted the potential of LRCC, it is essential to acknowledge the challenges in both research and practical applications. To enhance existing methodologies and guide future investigations, several challenges and research priorities are identified below:

(1) In this study, the mismatch between LR and matrix properties led to single localized fracture in the matrix. Improvements in composite design, such as adopting stiffer materials such as steel, or optimizing the proportion and positioning of reinforcement, could potentially facilitate flexural-hardening behavior with spread-out multiple cracks. This is also one of the design flexibilities that 3D-printed lattice reinforcements offer – to enable precise control over the placement of the reinforcement material and allow it to be optimized for specific loading conditions. Future research should focus on material optimization and reinforcement strategies, ensuring improved compatibility between LR and matrix to optimize composite performance. Parametric design and topology optimization could be powerful tools for this purpose.

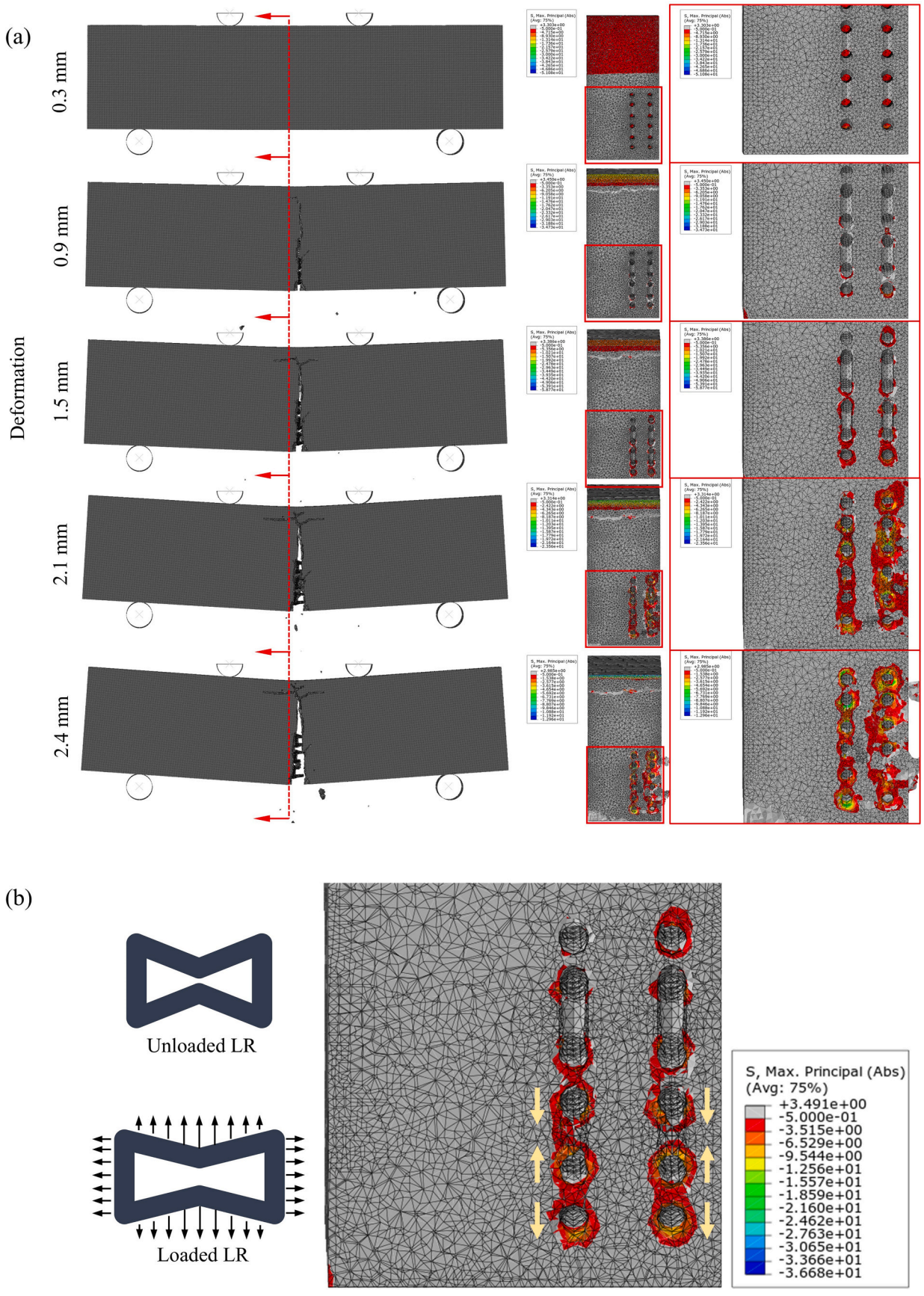

Fig. 19. (a) Evolution of deformed shapes and contour plots of maximal principal stresses in the matrix, and (b) contour plot at 1.8 mm deformation in RE-S-LRCC simulation. Contour colors indicate compressive stresses below − 0.5 MPa, and gray indicates higher stresses.

(2) More extensive research is required to fully understand and optimize the bonding between LR and the surrounding matrix, as interfacial interactions significantly affect failure mechanisms. While debonding allows LR to fully utilize its deformation capacity, it can also compromise the overall integrity of the composite. Therefore, design optimization for LRCC needs to carefully balance these competing factors – enabling controlled debonding to harness the benefits of lattice structures, while simultaneously ensuring the structural integrity necessary to achieve the desired performance. Furthermore, this may involve exploring the interaction mechanisms of various LR materials, e.g., steel, with the matrix. The use of 3D-printed steel reinforcement is a promising direction, which offers the potential to combine traditional materials with advanced manufacturing techniques and functional lattice structures. However, integrating 3D-printed steel LR into cementitious composites will necessitate a new understanding of the interfacial properties typically seen in traditional reinforced concrete. In addition, it should be noted that although the auxetic behavior of the reinforcement may reduce the risk of debonding, the associated lateral expansion could potentially affect the integrity of the surrounding mortar. In the present study, this concern did not arise, as the resin used for the lattice had significantly lower stiffness than the cementitious matrix. However, this effect warrants careful consideration when stiffer reinforcement materials, such as metals, are employed.

(3) The lattice reinforcement strategy proposed in this study shows promising scalability. Although this work serves as a proof-of-concept using small-scale specimens, recent advancements in large-format metal additive manufacturing, such as wire arc additive manufacturing, have enabled the fabrication of meter-scale metallic structures. Moreover, conventional fabrication techniques, including stamping, bending, or welding of metal strips into repeatable lattice units, offer cost-effective alternatives for large-scale production. These developments highlight the potential of applying lattice-reinforced cementitious composites in full-scale structural elements, thereby enhancing their practical relevance. Nevertheless, scaling up will require further investigation into full-scale manufacturing, long-term durability, and cost-efficiency.

CRediT authorship contribution statement

Wen Zhou: Writing – original draft, Validation, Methodology, Investigation, Formal analysis, Data curation, Conceptualization. **Rowin J.M. Bol:** Formal analysis, Writing – original draft. **Yubao Zhou:** Writing – review & editing, Data curation. **Zhaozheng Meng:** Writing – review & editing, Investigation. **Yading Xu:** Writing – review & editing, Investigation. **Jinbao Xie:** Writing – review & editing, Investigation. **Branko Šavija:** Writing – review & editing, Supervision, Funding acquisition.

Declaration of competing interest

The authors declare that they have no known competing financial interests or personal relationships that could have appeared to influence the work reported in this paper.

Acknowledgments

Financial support by the European Research Council (ERC) within the framework of the ERC Starting Grant Project "Auxetic Cementitious Composites by 3D printing (ACC-3D)", Grant Agreement Number 101041342, is acknowledged. Views and opinions expressed are however those of the author(s) only and do not necessarily reflect those of the European Union or the European Research Council. Neither the European Union nor the granting authority can be held responsible for them.

Appendix

Table A1
Input parameters for high-elongation resin.

Yield Stress (MPa)	Plastic Strain
12	0
13	0.00323
14	0.0114
15	0.037343
16	0.07063
17	0.108933
18	0.146
19	0.179
19.3595	0.1885
20	0.212
21	0.245
22	0.278
23	0.311
24	0.344
25	0.377
25.9697	0.4
27	0.433
28	0.466
29	0.499
30	0.532
31	0.565
32	0.598
33	0.631
34	0.664
35	0.697
36	0.73

(*continued on next page*)

Table A1 (*continued*)

Yield Stress (MPa)	Plastic Strain
37	0.763
38	0.796
38.1212	0.8

Data availability

Data will be made available on request.

References

[1] X. Zhang, P. Liu, L. Wu, Study on flexural properties of 3D printing functionally graded lattice structure cement composites, Mater. Lett. 375 (2024) 137231, https://doi.org/10.1016/j.matlet.2024.137231.

[2] E.O. Momoh, A. Jayasinghe, M. Hajsadeghi, R. Vinai, K.E. Evans, P. Kripakaran, J. Orr, A state-of-the-art review on the application of auxetic materials in cementitious composites, Thin-Walled Struct. 196 (2024) 111447, https://doi.org/10.1016/j.tws.2023.111447.

[3] C. Tang, J. Liu, J. Qiao, Y. Wei, C. Shi, W. Hao, The preparation and axial compressive properties of 3D-printed polymer lattice-reinforced cementitious composite columns, J. Build. Eng. 97 (2024) 110770, https://doi.org/10.1016/j.jobe.2024.110770.

[4] C. Tang, J. Liu, W. Hao, Y. Wei, Flexural properties of 3D printed graded lattice reinforced cementitious composites using digital image correlation, Mater. Des. 227 (2023) 111734, https://doi.org/10.1016/j.matdes.2023.111734.

[5] W. Hao, J. Liu, H. Kanwal, Compressive properties of cementitious composites reinforced by 3D printed PA 6 lattice, Polym. Test. 117 (2023) 107811, https://doi.org/10.1016/j.polymertesting.2022.107811.

[6] K.E. Evans, Auxetic polymers: a new range of materials, Endeavour 15 (1991) 170–174, https://doi.org/10.1016/0160-9327(91)90123-S.

[7] S. Yuan, F. Shen, J. Bai, C.K. Chua, J. Wei, K. Zhou, 3D soft auxetic lattice structures fabricated by selective laser sintering: TPU powder evaluation and process optimization, Mater. Des. 120 (2017) 317–327, https://doi.org/10.1016/j.matdes.2017.01.098.

[8] J. Wu, O. Sigmund, J.P. Groen, Topology optimization of multi-scale structures: a review, Struct. Multidiscip. Optim. 63 (2021) 1455–1480, https://doi.org/10.1007/s00158-021-02881-8.

[9] E. Etemadi, M. Hosseinabadi, F. Scarpa, H. Hu, Design, FDM printing, FE and theoretical analysis of auxetic structures consisting of arc-shaped and Dumbell-shaped struts under quasi-static loading, Compos. Struct. 326 (2023) 117602, https://doi.org/10.1016/j.compstruct.2023.117602.

[10] A. Bouteldja, M.A. Louar, L. Hemmouche, L. Gilson, A. Miranda-Vicario, L. Rabet, Experimental investigation of the quasi-static and dynamic compressive behavior of polymer-based 3D-printed lattice structures, Int. J. Impact Eng. 180 (2023) 104640, https://doi.org/10.1016/j.ijimpeng.2023.104640.

[11] Y. Xu, B. Šavija, Development of strain hardening cementitious composite (SHCC) reinforced with 3D printed polymeric reinforcement: Mechanical properties, Compos. Part B Eng. 174 (2019) 107011, https://doi.org/10.1016/j.compositesb.2019.107011.

[12] Y. Xu, Z. Meng, R.J.M. Bol, B. Šavija, Spring-like behavior of cementitious composite enabled by auxetic hyperelastic frame, Int. J. Mech. Sci. 275 (2024) 109364, https://doi.org/10.1016/j.ijmecsci.2024.109364.

[13] R.J.M. Bol, Y. Xu, B. Šavija, Printing path-dependent two-scale models for 3D printed planar auxetics by material extrusion, Addit. Manuf. 89 (2024) 104293, https://doi.org/10.1016/j.addma.2024.104293.

[14] R. Raj, M. Jiyalal Prajapati, J.-T. Tsai, A. Kumar, J.-Y. Jeng, Design and additive manufacturing of novel hybrid lattice metamaterial for enhanced energy absorption and structural stability, Mater. Des. 245 (2024) 113268, https://doi.org/10.1016/j.matdes.2024.113268.

[15] R. Rodríguez-Aparicio, J.M. Alegre, W.M.H. Verbeeten, M. Lorenzo-Bañuelos, I. I. Cuesta, Methodology to predict mechanical properties of PA-12 lattice structures manufactured by powder bed fusion, Addit. Manuf. 78 (2023) 103864, https://doi.org/10.1016/j.addma.2023.103864.

[16] S. Li, T. Wang, S. Chen, Y. Li, Y. Zou, B. Cao, J. Hu, X. Tan, B. Wang, Compressive properties and biocompatibility of additively manufactured lattice structures by using bioactive materials, Thin-Walled Struct. 205 (2024) 112469, https://doi.org/10.1016/j.tws.2024.112469.

[17] U.A. Dar, H.H. Mian, M. Abid, A. Topa, M.Z. Sheikh, M. Bilal, Experimental and numerical investigation of compressive behavior of lattice structures manufactured through projection micro stereolithography, Mater. Today Commun. 25 (2020) 101563, https://doi.org/10.1016/j.mtcomm.2020.101563.

[18] J. Zhang, X. Chen, Y. Sun, Y. Wang, L. Bai, Sound-absorption and mechanical properties of multisheet Gyroid lattice structures by stereolithography, Compos. Struct. 325 (2023) 117589, https://doi.org/10.1016/j.compstruct.2023.117589.

[19] J.-H. Kang, K. Sakthiabirami, K.-J. Jang, J.-G. Jang, G.-J. Oh, C. Park, J.G. Fisher, S.-W. Park, Mechanical and biological evaluation of lattice structured hydroxyapatite scaffolds produced via stereolithography additive manufacturing, Mater. Des. 214 (2022) 110372, https://doi.org/10.1016/j.matdes.2021.110372.

[20] Z. Meng, Y. Xu, J. Xie, W. Zhou, R.J.M. Bol, Q. Liu, B. Šavija, Unraveling the reinforcing mechanisms for cementitious composites with 3D printed multidirectional auxetic lattices using X-ray computed tomography, Mater. Des. 246 (2024) 113331, https://doi.org/10.1016/j.matdes.2024.113331.

[21] K.E. Evans, A. Alderson, Auxetic materials: Functional materials and structures from lateral thinking!, Adv. Mater. 12 (2000) 617–628, https://doi.org/10.1002/(SICI)1521-4095(200005)12:9<617::AID-ADMA617>3.0.CO;2-3.

[22] X. Xue, C. Lin, F. Wu, Z. Li, J. Liao, Lattice structures with negative Poisson's ratio: a review, Mater. Today Commun. 34 (2023) 105132, https://doi.org/10.1016/j.mtcomm.2022.105132.

[23] A. Spadoni, M. Ruzzene, Elasto-static micropolar behavior of a chiral auxetic lattice, J. Mech. Phys. Solids 60 (2012) 156–171, https://doi.org/10.1016/j.jmps.2011.09.012.

[24] D. Prall, R.S. Lakes, Properties of a chiral honeycomb with a poisson's ratio of — 1, Int. J. Mech. Sci. 39 (1997) 305–314, https://doi.org/10.1016/S0020-7403(96)00025-2.

[25] T. Zahra, M. Asad, J. Thamboo, Flexural behaviour of cementitious composites embedded with 3D printed re-entrant chiral auxetic meshes, Smart Mater. Struct. 33 (2024) 025011, https://doi.org/10.1088/1361-665X/ad1b24.

[26] X.G. Zhang, X. Ren, W. Jiang, X.Y. Zhang, C. Luo, Y. Zhang, Y.M. Xie, A novel auxetic chiral lattice composite: experimental and numerical study, Compos. Struct. 282 (2022) 115043, https://doi.org/10.1016/j.compstruct.2021.115043.

[27] C. Iantaffi, E. Bele, D. McArthur, P.D. Lee, C.L.A. Leung, Auxetic response of additive manufactured cubic chiral lattices at large plastic strains, Mater. Des. 233 (2023) 112207, https://doi.org/10.1016/j.matdes.2023.112207.

[28] X.C. Teng, X. Ren, Y. Zhang, W. Jiang, Y. Pan, X.G. Zhang, X.Y. Zhang, Y.M. Xie, A simple 3D re-entrant auxetic metamaterial with enhanced energy absorption, Int. J. Mech. Sci. 229 (2022) 107524, https://doi.org/10.1016/j.ijmecsci.2022.107524.

[29] L. Yang, O. Harrysson, H. West, D. Cormier, Mechanical properties of 3D re-entrant honeycomb auxetic structures realized via additive manufacturing, Int. J. Solids Struct. 69–70 (2015) 475–490, https://doi.org/10.1016/j.ijsolstr.2015.05.005.

[30] W. Liu, N. Wang, T. Luo, Z. Lin, In-plane dynamic crushing of re-entrant auxetic cellular structure, Mater. Des. 100 (2016) 84–91, https://doi.org/10.1016/j.matdes.2016.03.086.

[31] J.N. Grima, K.E. Evans, Auxetic behavior from rotating squares, J. Mater. Sci. Lett. 19 (2000) 1563–1565, https://doi.org/10.1023/A:1006781224002.

[32] J.N. Grima, K.E. Evans, Auxetic behavior from rotating triangles, J. Mater. Sci. 41 (2006) 3193–3196, https://doi.org/10.1007/s10853-006-6339-8.

[33] P. Dobnik Dubrovski, N. Novak, M. Borovinšek, M. Vesenjak, Z. Ren, In-plane behavior of auxetic non-woven fabric based on rotating square unit geometry under tensile load, Polymers 11 (2019) 1040, https://doi.org/10.3390/polym11061040.

[34] T.A. Schaedler, W.B. Carter, Architected cellular materials, Annu. Rev. Mater. Res. 46 (2016) 187–210, https://doi.org/10.1146/annurev-matsci-070115-031624.

[35] Y. Xu, E. Schlangen, M. Luković, B. Šavija, Tunable mechanical behavior of auxetic cementitious cellular composites (CCCs): Experiments and simulations, Constr. Build. Mater. 266 (2021) 121388, https://doi.org/10.1016/j.conbuildmat.2020.121388.

[36] M. Asad, M. Dhanasekar, T. Zahra, D. Thambiratnam, Impact mitigation of masonry walls with carbon fibre and Auxetic fibre composite renders – a numerical study, Structures 28 (2020) 2733–2751, https://doi.org/10.1016/j.istruc.2020.09.047.

[37] X.G. Zhang, W. Jiang, Y. Zhang, C. Luo, X.Y. Zhang, D. Han, J. Hao, X.C. Teng, Y. M. Xie, X. Ren, Energy absorption properties of composite tubes with hexagonal and re-entrant honeycomb fillers, Constr. Build. Mater. 356 (2022) 129298, https://doi.org/10.1016/j.conbuildmat.2022.129298.

[38] F. Scarpa, L.G. Ciffo, J.R. Yates, Dynamic properties of high structural integrity auxetic open cell foam, Smart Mater. Struct. 13 (2003) 49, https://doi.org/10.1088/0964-1726/13/1/006.

[39] S. Yang, C. Qi, D. Wang, R. Gao, H. Hu, J. Shu, A comparative study of ballistic resistance of sandwich panels with aluminum foam and auxetic honeycomb cores, Adv. Mech. Eng. 2013 (2013), https://doi.org/10.1155/2013/589216.

[40] P. Subramani, S. Rana, D.V. Oliveira, R. Fangueiro, J. Xavier, Development of novel auxetic structures based on braided composites, Mater. Des. 61 (2014) 286–295, https://doi.org/10.1016/j.matdes.2014.04.067.

[41] T. Zahra, M. Dhanasekar, Characterisation of cementitious polymer mortar – Auxetic foam composites, Constr. Build. Mater. 147 (2017) 143–159, https://doi.org/10.1016/j.conbuildmat.2017.04.151.

[42] N. Novak, L. Krstulović-Opara, Z. Ren, M. Vesenjak, Compression and shear behaviour of graded chiral auxetic structures, Mech. Mater. 148 (2020) 103524, https://doi.org/10.1016/j.mechmat.2020.103524.

[43] G. Zhao, Y. Fan, C. Tang, Y. Wei, W. Hao, Preparation and compressive properties of cementitious composites reinforced by 3D printed cellular structures with a

negative Poisson's ratio, Dev. Built Environ. 17 (2024) 100362, https://doi.org/10.1016/j.dibe.2024.100362.
[44] Y. Xu, B. Šavija, Auxetic cementitious composites (ACCs) with excellent compressive ductility: experiments and modeling, Mater. Des. 237 (2024) 112572, https://doi.org/10.1016/j.matdes.2023.112572.
[45] N.K. Choudhry, T.K. Nguyen, V. Nguyen-Van, B. Panda, P. Tran, Auxetic lattice reinforcement for tailored mechanical properties in cementitious composite: experiments and modelling, Constr. Build. Mater. 438 (2024) 137252, https://doi.org/10.1016/j.conbuildmat.2024.137252.
[46] G. Tzortzinis, A. Gross, S. Gerasimidis, Auxetic boosting of confinement in mortar by 3D reentrant truss lattices for next generation steel reinforced concrete members, Extreme Mech. Lett. 52 (2022) 101681, https://doi.org/10.1016/j.eml.2022.101681.
[47] M. Chen, Z. Chen, Y. Xuan, T. Zhang, M. Zhang, Static and dynamic compressive behaviour of 3D printed auxetic lattice reinforced ultra-high performance concrete, Cem. Concr. Compos. 139 (2023) 105046, https://doi.org/10.1016/j.cemconcomp.2023.105046.
[48] J. Liu, H. Kanwal, C. Tang, W. Hao, Study on flexural properties of 3D printed lattice-reinforced concrete structures using acoustic emission and digital image correlation, Constr. Build. Mater. 333 (2022) 127418, https://doi.org/10.1016/j.conbuildmat.2022.127418.
[49] B. Xie, R. Tian, H. Zhao, T. Ye, Y. Zhang, N. Hu, Controlling crack propagation in layered beams with architected lattice-reinforced composite interlayer designs, Constr. Build. Mater. 426 (2024) 136174, https://doi.org/10.1016/j.conbuildmat.2024.136174.
[50] R. Barhemat, S. Mahjoubi, W. Meng, Y. Bao, Automated design of architectured polymer-concrete composites with high specific flexural strength and toughness using sequential learning, Constr. Build. Mater. 449 (2024) 138311, https://doi.org/10.1016/j.conbuildmat.2024.138311.
[51] J.A. Rosewitz, H.A. Choshali, N. Rahbar, Bioinspired design of architected cement-polymer composites, Cem. Concr. Compos. 96 (2019) 252–265, https://doi.org/10.1016/j.cemconcomp.2018.12.010.
[52] B. Salazar, P. Aghdasi, I.D. Williams, C.P. Ostertag, H.K. Taylor, Polymer lattice-reinforcement for enhancing ductility of concrete, Mater. Des. 196 (2020) 109184, https://doi.org/10.1016/j.matdes.2020.109184.
[53] P. Dong, J. Hu, C. Lin, W. Ding, J. Liu, Y. Liu, Topology-optimized lattice enhanced cementitious composites, Mater. Des. 244 (2024) 113155, https://doi.org/10.1016/j.matdes.2024.113155.
[54] B. Xie, X. Li, X. Zhao, N. Hu, Tunable properties and responses of architected lattice-reinforced cementitious composite components induced by versatile cell topology and distributions, Compos. Struct. 312 (2023) 116850, https://doi.org/10.1016/j.compstruct.2023.116850.
[55] S. Qin, S. Cao, E. Yilmaz, J. Li, Influence of types and shapes of 3D printed polymeric lattice on ductility performance of cementitious backfill composites, Constr. Build. Mater. 307 (2021) 124973, https://doi.org/10.1016/j.conbuildmat.2021.124973.
[56] P. Dong, W. Ding, H. Yuan, Q. Wang, 3D-printed polymeric lattice-enhanced sustainable municipal solid waste incineration fly ash alkali-activated cementitious composites, Dev. Built Environ. 12 (2022) 100101, https://doi.org/10.1016/j.dibe.2022.100101.
[57] ASTM D638-22 Standard Test Method for Tensile Properties of Plastics, (2022).
[58] M. Saeedifar, D. Zarouchas, Damage characterization of laminated composites using acoustic emission: a review, Compos. Part B Eng. 195 (2020) 108039, https://doi.org/10.1016/j.compositesb.2020.108039.
[59] N. Holsamudrkar, S. Banerjee, Acoustic emission (AE) based health monitoring of RC beams strengthened with mechanically anchored hybrid fiber reinforced cementitious matrix (FRCM) system, Case Stud. Constr. Mater. 21 (2024) e03773, https://doi.org/10.1016/j.cscm.2024.e03773.
[60] Z. Chen, G. Zhang, R. He, Z. Tian, C. Fu, X. Jin, Acoustic emission analysis of crack type identification of corroded concrete columns under eccentric loading: a comparative analysis of RA-AF method and Gaussian mixture model, Case Stud. Constr. Mater. 18 (2023) e02021, https://doi.org/10.1016/j.cscm.2023.e02021.
[61] D.D. Mandal, M. Bentahar, A. El Mahi, A. Brouste, R. El Guerjouma, S. Montresor, F.-B. Cartiaux, Acoustic emission monitoring of progressive damage of reinforced concrete T-beams under four-point bending, Materials 15 (2022) 3486, https://doi.org/10.3390/ma15103486.
[62] J. Chang, Y. Yao, K. Liu, Y. Wang, M. Yan, Y. Bao, Damage assessment of concrete beams repaired with basalt fiber-reinforced polymer sheets through digital image correlation and acoustic emission, Case Stud. Constr. Mater. 20 (2024) e03044, https://doi.org/10.1016/j.cscm.2024.e03044.
[63] W. Zhou, Y. Xu, Z. Meng, J. Xie, Y. Zhou, E. Schlangen, B. Šavija, Filament stitching: an architected printing strategy to mitigate anisotropy in 3D-printed engineered cementitious composites (ECC), Cem. Concr. Compos. 160 (2025) 106044, https://doi.org/10.1016/j.cemconcomp.2025.106044.
[64] Y. Zhou, M. Liang, X. Yue, Deep residual learning for acoustic emission source localization in a steel-concrete composite slab, Constr. Build. Mater. 411 (2024) 134220, https://doi.org/10.1016/j.conbuildmat.2023.134220.
[65] T. Pan, Y. Zheng, Y. Zhou, W. Luo, X. Xu, C. Hou, Y. Zhou, Damage pattern recognition for corroded beams strengthened by CFRP anchorage system based on acoustic emission techniques, Constr. Build. Mater. 406 (2023) 133474, https://doi.org/10.1016/j.conbuildmat.2023.133474.
[66] Y. Zheng, Y. Zhou, Y. Zhou, T. Pan, L. Sun, D. Liu, Localized corrosion induced damage monitoring of large-scale RC piles using acoustic emission technique in the marine environment, Constr. Build. Mater. 243 (2020) 118270, https://doi.org/10.1016/j.conbuildmat.2020.118270.
[67] M.U. Hanif, S.-Y. Seo, H. Van Tran, K. Senghong, Monitoring and characterizing the debonding in CFRP retrofitted RC beams using acoustic emission technology, Dev. Built Environ. 14 (2023) 100141, https://doi.org/10.1016/j.dibe.2023.100141.
[68] Y. Xu, H. Zhang, Y. Gan, B. Šavija, Cementitious composites reinforced with 3D printed functionally graded polymeric lattice structures: experiments and modelling, Addit. Manuf. 39 (2021) 101887, https://doi.org/10.1016/j.addma.2021.101887.